



### **Science Arts & Métiers (SAM)**

is an open access repository that collects the work of Arts et Métiers Institute of Technology researchers and makes it freely available over the web where possible.

This is an author-deposited version published in: <https://sam.ensam.eu>  
Handle ID: <http://hdl.handle.net/10985/25222>

#### **To cite this version :**

Ijaz AKBAR, Mourad EL HADROUZ, Mohamed EL MANSORI, Mostapha TARFAOUI -  
Thermomechanical shape memory testing of 4D printed novel material rhombus-shape structure -  
Applied Materials Today - Vol. 33, p.101876 - 2023

Any correspondence concerning this service should be sent to the repository

Administrator : [scienceouverte@ensam.eu](mailto:scienceouverte@ensam.eu)



# Thermomechanical shape memory testing of 4D printed novel material rhombus-shape structure

Ijaz Akbar<sup>a,\*</sup>, Mourad El Hadrouz<sup>a</sup>, Mohamed El Mansori<sup>b,c</sup>, Mostapha Tarfaoui<sup>d</sup>

<sup>a</sup> Arts et Metiers Institute of Technology, MSMP, HESAM Université, F-51006, Châlons-en-Champagne, France

<sup>b</sup> Arts et Metiers Institute of Technology, MSMP, HESAM Université, F-13617 Aix-en-Provence, France

<sup>c</sup> Texas A&M Engineering Experiment Station, College Station, TX 77843, USA

<sup>d</sup> École nationale supérieure de techniques avancées (ENSTA) Bretagne, 29200 Brest, France

## ABSTRACT

### Keywords:

SMP's thermomechanical cycle

Shape memory characteristics

Shape memory effects

Printing parameters

4D printing

4D printing of functional energy generation/absorption structures by material extrusion technique can capitalize on the exciting applications in intelligent damping devices and patterns to deform spontaneously. This paper investigated the capitalization of this acquired knowledge by studying the shape memory effects of a functional rhombus shape structure. Initially, the shape memory characteristics of energy absorption and dissipation capacity were analyzed using dynamic mechanical testing to develop databases to gather thermophysical data before expressing the material behavior and recovery performances of printed shape memory structures. Then a complete thermomechanical cycle (shape programming and recovery) on 4D printed amorphous and semi-crystalline shape memory polymers exhibited deep insights into shape memory performance. The performance factors (i.e., recovery and fixity ratios) are influenced by variable printing parameters (i.e., layer height, printing temperature, and speed) and stimuli-based testing conditions. Results reveal both materials have significant shape memory effects with a maximum recovery ratio of up to  $92.30 \pm 0.32\%$  from the programmed configuration. The amorphous polymer was extremely affected by printing temperature, whilst the semi-crystalline was influenced heavily by the interaction of all three parameters. Finally, shape memory effects predicted by a high-order design model and compared with experimental results showed negligible error. The analyses and assessments presented in this paper are adequate to understand the shape memory behavior under process control parameters to establish a data-driven model of a 4D printed semi-crystalline and amorphous polymer reactive to thermal stimuli.

## 1. Introduction

4D printing is a novel dimension of 3D printed shape memory materials (SMMs) when they are subject to stimuli and time. 4D printing (4DP) of intelligent and lightweight structures is gaining attention thanks to their highly autonomous functionality in response to their shape memory properties. The SMMs governed by 4DP are prone to high recoverable strain, super elastic behavior, easy shape transformation, and high recovery ratios [1–3]. 4D printing is eventually associated with the effects of “shape memory” that 3D printed shape memory material based structures evolve over external stimuli and time [4,5]. The 2-way configuration from an initial to temporarily transformed shape and then recovered back to the initial shape, is termed reversibility of SMMs. The shape memory of SMMs is driven by induced/stored/locked residual

stress/strains during the cooling phase firstly, in the printing process, and later during the shape programming for temporary configurations [6,7].

Earlier investigations have mainly reported the shape memory effects (SMEs) of shape memory polymers (SMPs) fabricated from injection molding or casted sheets/pellets rather than 3D printing processes [8,9]. Although recent studies have elaborated on the successful printing of SMPs using a material extrusion process namely Fused Filament Fabrication (FFF) based 3D printers [10], however, the effects of material variability and printing parameters on SMEs of rhombus-shape-structure (RSS) remain ambiguous to date [11]. Testoni et al. [12] designed and validated the 4D printing applications of an active complaint hinge for satellite-orientable solar panels. The meta-material combination of SMPs and shape memory alloys (SMAs) enabled

\* Corresponding author.

E-mail address: [ijaz.akbar@ensam.eu](mailto:ijaz.akbar@ensam.eu) (I. Akbar).

the controlled memory actuation of the hinge with an angular position between  $-90$  to  $+90^\circ$  without consuming external energy. D'Elia et al. [13] integrated a graphene network ( $< 1$  wt%) into the SMP matrix to enable its electrical stimuli and increase the compressive strength for 4D printing. Their composite memory material showed fast and higher shape recovery as compared to pure SMPs on applied joule-heating as stimuli. Similarly, N Namvar et al. [14] designed and fabricated three metamaterial lattice structures using the FFF printing process to examine their energy absorption and dissipation capacity for 4D printing. They found a re-entrant auxetic unit-cells PLA structure prone to maximum energy absorption and recovery ability due to its unique cell deformation mechanism.

Zeng et al. [11] designed and presented the energy absorption capacity of the honeycomb cellular structures for 4D printing applications without fracture while performing the in-plan and out-of-plane compression/recovery cycling. Akbar et al. [10] discussed the distortion-free 4D printing of amorphous SMP using material extrusion technology (FFF) while optimizing the printing parameters (such as layer thickness, bed temperature, and printing speed) that directly affect the dimensional accuracy and stability of SMPs. Aberoumand et al. [15] investigated the SMEs of thermo-responsive PET-G produced by a FFF 3D printer and indicated that a higher pre-imposed/stored strain contributes towards higher shape recovery ratios. However, this concept is limited to a specific percentage of the deformation before the permanent locking of the structure concerning geometric constraints [16]. In addition, Li et al. [17] investigated the role of loading rate (i.e., 0.1%/s, 0.5%/s, and 2%/s) and peak nominal strains (i.e., 10%, 25%, 50%, 75%, and 100%) on shape memory effects using a dogbone structure without varying the printing parameters, geometric complexity, and material properties. They reported the shape recovery ratio decreased with the increase in loading rate and the number of shape memory cycles (SMCs). Mehrpouya et al. [18] reported the influence of printing parameters on SMEs, saying a higher layer thickness of 0.3 mm maximized shape recovery by up to 90 percent. In addition, Mehrpouya et al. [3] investigated the influence of printing temperature and speed on shape memory PLA, they indicated increasing the temperature from  $210^\circ\text{C}$  to  $230^\circ\text{C}$  presented no further increase in shape memory performance factors and an increase in printing speed decreased those factors. However, stimuli-responsive shape morphing of such intricate and reconfigurable objects by 4D printing remains a significant challenge.

The latest publications discussed the potential of shape memory properties of different 3D/4D printed polymers such as PLA, PCL, PETG, etc. [7,15,16,19]. These studies are providing the conceptual frameworks to prove the concept of 4D printing, without presenting the deep insights of SMP depending on structural design, materials variability, and optimal printing conditions which can eliminate the need for physical aging and optimize memory performance. Accordingly, the outcomes of two key drivers can accelerate the wide range of applications of SMPs, the first is SMEs which are sensitive to the fabrication process, effective stimuli, and choice of materials to enhance the performance factors such as shape recovery and fixity ratios. The second key driver is the choice of fabrication process parameters affecting the extrusion rate and quality, layers bonding, layers orientations, level of porosity, and surface quality [7,20]. Intense investigation into these drivers responsible for the successful attainment of 4D printed rhombus-shape-structure is missing in the literature [21,22]. Furthermore, the intricate intelligent energy-absorbing structures [23] and their accurate thermomechanical SMC considering an amorphous and semi-crystalline polymeric network have not been discussed for 4D printing applications.

Thereafter this paper investigates the SMEs of 3D-printed complex design structures reactive to thermal stimuli and printing parameters. The samples were prepared using a FFF 3D printer considering multiple designs of the experiment (DOE) predicted parameters. The polymer's memory behavior was investigated inside a controlled environmental chamber (in total sixteen specimens), and the accurate measures of the

deformation mechanism were registered while using a non-contacting advanced video extensometer. Three critical printing parameters, such as layer thickness, printing speed, and nozzle temperature, were considered the major influencing factors that directly affect the induced pre-strain and residual stresses developed during the printing process which is significant for SMEs, such as shape recovery ratio ( $R_r$ ). Those functional responses of both SMPs determine the capacity of shape memory affected by the choice of printing parameters and collectively by the influence of the material's variability. Since variable printing parameters and material properties can generate heterogeneous and homogeneous induced strains, therefore the investigation of the best set of printing parameters was indispensable. Finally, the potential objective of the study is to optimize the shape memory performance factors (i.e.,  $R_r$  and  $R_f$ ) under an optimal set of printing parameters. The resulting influences on both SMPs were studied through percentage shape recovery ratio analyses.

Since the SMEs of RSS are associated with the strain energy absorption during shape deformation and release for recovery, therefore, initially the thermal stimulation-based performance parameters of both SMPs were investigated under the data collection analytics section. Secondly, the framework of the physical analysis section presents a description of the induced 4D printed shape memory response under thermomechanical extreme conditions, which stimulate their end use, together with empirical, and physical information concerning their additive manufacturing method. Finally, the resulting section elaborated on the shape memory effects (performance) of two SMP materials. Overall, the study provides interesting qualitative and quantitative insights into the SMEs of the 4D printed rhombus shape structure.

## 2. Materials and methods

### 2.1. Smart materials

The SMPs used in this research are sensitive to thermal stimuli [23] to trigger their shape-memory behavior and possess distinct thermal properties. Shape memory properties mainly reside in the two phases of such reversible SMPs, namely the hard or glassy phase, and the soft or rubbery phase, individually [24]. A polyurethane-type amorphous SMP (A-SMP) filament was produced by SMP Technologies Co., Ltd (Japan) and used for the 4D printing of RSS in this paper. This material can withstand a rubbery modulus up to 20 MPa above the glassy transition range which indicates a better selection of material to discuss the applications of mini engineering and intelligent biomedical devices used in constrained conditions such as human skin. The second 4D printing SMP filament is a semi-crystalline polylactic acid type SMP fabricated by Shenzhen eSun Industrial Co., Ltd (China) and termed C-SMP in this study. This time, the C-SMP material is presenting its first study to analyze its shape memory properties considering the effects of printing parameters under precise thermomechanical shape programming and recovery cycles.

### 2.2. Data collection analytics

#### 2.2.1. Dynamic mechanical analysis

For instance, the vital strain energy storage factors, such as temperature-dependent storage modulus, loss modulus,  $\tan\delta$  (loss factor), and elastic modulus at glassy and rubbery phases are precisely analyzed using a dynamic mechanical analyzer (DMA). These factors are considered an important criterion to define the shape programming temperatures, energy absorbing/dissipation capacity of RSS, relaxation peak, and reversibility effect to recover back during the thermomechanical cycles [8,25]. The melting transition temperature of C-SMP will be called the transition temperature ( $\theta_g$ ) for simple communication in this paper, or even due to the amorphous part the  $\theta_g$  exists as well.  $\theta_g$  is a complex procedure not fully understood despite several theories [1,



25]. Therefore, the analysis of material behavior especially, related to shape memory characteristics, such as the energy dissipation factor  $\tan(\delta)$  to estimate  $\theta_g$  and energy absorption measure (storage modulus) to estimate the peak-strain capacity is crucial.

A DMA instrument with a rotatable measuring head (DMA 1) by Mettler Toledo was used to characterize the temperature and frequency-dependent dynamic mechanical properties of both SMPs in a standard tension mode. The storage modulus is considered the backbone of shape memory properties since it reflects the amount of energy a material can store according to the material's viscoelastic behavior. Therefore, storage modulus (storage modulus = stress/dissipated energy ratio) is a key factor to facilitate the SMEs of SMPs [26]. FFF based 3D printed beam-like specimens of A-SMP and C-SMP of  $15 \times 3.3 \times 1.5 \text{ mm}^3$  were analyzed at a heating rate of  $1^\circ\text{C min}^{-1}$  until  $160^\circ\text{C}$  and at different forcing frequencies of 1 Hz and 10 Hz with a peak-to-peak amplitude of 0.05% according to "ASTM D4065–12 dynamic mechanical properties standard" to see the relevant effects on the thermomechanical properties [25,27]. Due to distinct SMPs, similar size samples were printed following the individual optimal printing parameters given in Table 1, where the 90/0 infill type illustrates the layers deposition direction. These printing parameters to fabricate the DMA samples were chosen to maintain a compromise towards adhesion to the plateau, bonding between adjacent layers, mechanical properties, and successful printing of SMPs, respectively [28]. Accordingly, the SMP's successful printing practices recommended by Akbar et al. [10] suggested, the plateau temperature of both SMPs should be selected according to their  $\theta_g$  sensitivity or even below.

Fig. 1ab shows the evolution of the C-SMP and Fig. 1cd of A-SMP concerning their storage modulus and viscous modulus along with damping behavior ( $\tan \delta$ ) in the function of temperature and varying frequencies of 1 Hz and 10 Hz. The storage modulus of C-SMP was reported 2.8 GPa and 2.9 GPa around  $0^\circ\text{C}$  (glassy phase), 2.58 and 2.66 GPa at room temperature ( $20^\circ\text{C}$ ), whereas 2.56 MPa and 3.3 MPa around  $70^\circ\text{C}$  (rubbery phase) depending on 1 and 10 Hz forcing frequencies. However, the C-SMP modulus raised again between  $70$  and  $80^\circ\text{C}$  up to 115 MPa due to strong intermolecular forces, recrystallization, and plasticization effects. Meanwhile, the  $\theta_g$  value of the C-SMP given by the manufacturer is  $45^\circ\text{C}$  which corresponds to the lower transition temperature ( $L\theta_g$ ) of semicrystalline material. Whereas, the polymers belonging to  $\theta_g > 100^\circ\text{C}$  correspond to higher glass transition temperature ( $H\theta_g$ ) [4,26].

High elastic and storage moduli are prone to high  $\theta_g$  to activate the molecular mobility of the networks. Accordingly, the DMA analyses of the printed C-SMP specimens in this study portray a reasonable variation and fall between  $L\theta_g$  and  $H\theta_g$  range of  $50^\circ\text{C}$  while measured from  $\tan(\delta)$  peaks. Whereas a  $40 - 44^\circ\text{C}$   $\theta_g$  was found following a loss modulus peak that is near to one provided by the manufacturer and according to  $L\theta_g$  values of C-SMP. In contrast, the storage modulus of A-SMP at 1 and 10 Hz accounted for around 1.8 and 1.9 GPa at  $0^\circ\text{C}$ , 1.72 and 1.76 GPa at  $20^\circ\text{C}$  almost 35% less than C-SMP and comparable to DMA results reported by Bodaghi et al. [6]. Although, the modulus above  $\theta_g$  at  $70^\circ\text{C}$  seen as 30% better than C-SMP at 1 Hz and 10 Hz, respectively (Table 2).

**Table 1**  
Printing parameters for DMA/TMA characterization samples.

| Description                               | C-SMP | A-SMP |
|---|-------|-------|
| Printing temperature ( $^\circ\text{C}$ ) | 230   | 220   |
| Plateau temperature ( $^\circ\text{C}$ )  | 45    | 50    |
| Layer thickness (mm)                      | 0.2   | 0.2   |
| Printing speed (mm/s)                     | 45    | 45    |
| Infill density (%)                        | 100   | 100   |
| No. of shells                             | 1     | 1     |
| Filament diameter (mm)                    | 1.75  | 1.75  |
| Nozzle bore (mm)                          | 0.6   | 0.6   |
| Top/bottom solid layers                   | 2     | 2     |
| Infill type (rectilinear)                 | 90/0  | 90/0  |

The A-SMP has not shown any significant increase of modulus between  $70$  and  $80^\circ\text{C}$  because of their pure amorphous nature and poor intermolecular forces in contrast to C-SMP. Meanwhile, A-SMP shows a higher modulus around  $70^\circ\text{C}$  than C-SMP due to the presence of chain extenders, therefore, the values of  $\theta_g$  were observed bit higher than C-SMP. For the shape programming, the  $\theta_g$  values observed from  $\tan(\delta)$  peaks such as  $52 - 57^\circ\text{C}$  for C-SMP and  $57 - 61^\circ\text{C}$  for A-SMP at 1 Hz and 10 Hz enabled us to select a  $60^\circ\text{C}$  unique  $\theta_g$  for shape programming cycles of both SMPs. Similarly, for the recovery cycle, a  $\theta_g + 10$  ( $70^\circ\text{C}$ ) unique end recovery temperature was selected.

Overall, the crystallinity of C-SMP has a significant effect on storage modulus; presented in glassy and rubbery transition ranges in Table 2. The storage modulus of both SMPs reduced drastically 1000 times in the case of C-SMP and 434 times for A-SMP at 1 Hz near the rubbery zone at  $70^\circ\text{C}$ . The results are comparable with other amorphous and semi-crystalline polymers of similar nature [8,15]. The critical values of the storage and elastic modulus of both polymers from  $0$  to  $100^\circ\text{C}$  are reported in Table 2 for the researcher's community in case to develop constitutive laws or perform numerical modeling. Furthermore, the glassy and rubbery modulus at any relevant temperature can be calculated considering the relationship equation between storage and elastic modulus [6];  $E = E' \sqrt{1 + (\tan(\delta))^2}$  along with their  $\tan(\delta)$  factors drawn in Fig. 1. Initially, during the pure glassy range until  $30^\circ\text{C}$ , due to a very small  $\tan(\delta)$  value of  $< 0.1$  the elastic and storage values are quite similar to each other as shown in Table 2, however, this deviation increased 2–3 times around the glassy transition zone (about  $50^\circ\text{C}$ ). The elastic modulus in the pure glassy range ( $E_{pg}$ ), in the glassy transition range ( $E_{gt}$ ), and during the rubbery plateau ( $E_r$ ) correspond to different temperature ranges defining their subsequent effects on selected SMPs.

Overall, initially, the storage and loss modulus in the glassy zone get increased with the increase of the frequency level because going to a higher frequency means lowering the timescale of the applied stress that minimized the sample relaxation time, and the output modulus showed an increased value. In the glassy transition zone, both declined in the same plateau. Whereas  $E''$  (loss modulus) showed almost similar results around  $44^\circ\text{C}$  for 1 Hz and at  $48^\circ\text{C}$  for 10 Hz which is 2.327 MPa. However, the whole spectrum is complex until knowing the exact evolution of relaxation time. The  $\tan(\delta)$  of C-SMP went up to 0.38 which is very large compared to the common elastic materials, such as PLA and A-SMP discussed in this paper.

## 2.2.2. Thermomechanical analyzer (TMA)

A thermomechanical analyzer (TMA) assists to measure the change of dimensions in polymeric structures at zero applied stress but elevated temperatures during the heating cycles due to structural relaxation. The activation or movements of the atoms of the molecule causing the easy shape programming and recovery ratios are linked with the temperature change/rate and thermal strains in polymers [25]. The change in thermal expansion coefficient (CTE) during glassy and rubbery phases affects the SME properties, for example, the frozen stress formation during the cooling process is due to a change in thermal expansion, therefore, the influence of CTE in shape programming/recovery of both SMPs should not be ignored. In this regard, the TMA results shown in Fig. 2 were precisely examined while utilizing a Mettler TOLEDO TC100 MT intercooler-type thermomechanical analyzer. The effort is considered to measure the thermal expansion/shrinkage effects of both SMPs, especially their significance around glass transition and rubbery transition zones.

The TMA results presented in Fig. 2 reaffirm the DMA analysis. The heating and cooling cycles of both SMPs for the first and second heat were regulated at  $3^\circ\text{C.min}^{-1}$  and  $10^\circ\text{C.min}^{-1}$ . Whereas the first heat cycle was regulated until  $65^\circ\text{C}$  and the second cycle up to  $165^\circ\text{C}$ . As seen in Fig. 2a, in the case of the first heat of C-SMP a significant shrinkage leading to anisotropy is noticed around an average heat of  $40 - 50^\circ\text{C}$  of this polymer. This significant change is due to the relaxation

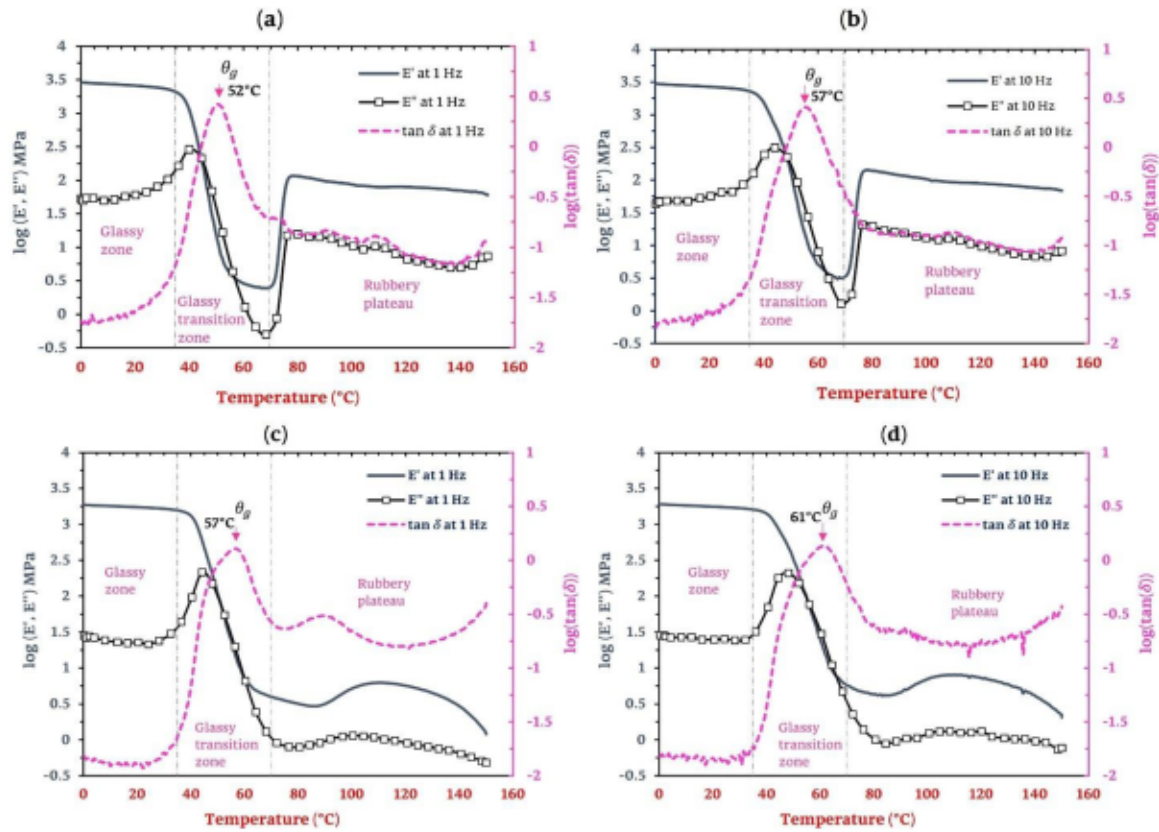


Fig. 1. Characterization of SMPs shape memory properties by DMA on C and A SMPs (a-b) Properties of C-SMP at 1 Hz and 10 Hz (c-d) Properties of A-SMP at 1 Hz and 10 Hz.

Table 2

Quantitative results of storage and elastic modulus of C and A SMPs in temperature response.

| Temperature<br>°C | C-SMP (MPa) |                      |          |                       | A-SMP (MPa) |                      |          |                        | Remarks  |
|-------------------|-------------|----------------------|----------|-----------------------|-------------|----------------------|----------|------------------------|----------|
|                   | E', 1Hz     | E <sub>g</sub> , 1Hz | E', 10Hz | E <sub>g</sub> , 10Hz | E', 1Hz     | E <sub>g</sub> , 1Hz | E', 10Hz | E <sub>g</sub> , 10 Hz |          |
| 0                 | 2862        | 2863                 | 2964     | 2964                  | 1863        | 1863                 | 1905     | 1905                   | $E_{pg}$ |
| 20                | 2582        | 2583                 | 2666     | 2667                  | 1728        | 1728                 | 1760     | 1761                   |          |
| 30                | 2350        | 2352                 | 2478     | 2479                  | 1642        | 1643                 | 1680     | 1680                   |          |
| 40                | 1131        | 1168                 | 1565     | 1583                  | 1310        | 1313                 | 1424     | 1425                   | $E_{gr}$ |
| 50                | 15.40       | 43                   | 126.10   | 212                   | 108.16      | 146.20               | 315.40   | 367.70                 |          |
| 60                | 2.89        | 3.23                 | 5.23     | 10.13                 | 7.23        | 10.22                | 25.88    | 42.84                  |          |
| 70                | 2.56        | 2.61                 | 3.30     | 3.50                  | 3.98        | 4.16                 | 5.74     | 6.71                   | $E_r$    |
| 80                | 114.30      | 115.30               | 139.05   | 140.50                | 3.18        | 3.27                 | 4.26     | 4.39                   |          |
| 90                | 96.60       | 97.60                | 118.42   | 119.45                | 3.16        | 3.30                 | 4.54     | 4.65                   |          |
| 100               | 86.30       | 86.90                | 103.17   | 103.99                | 5.18        | 5.30                 | 6.99     | 7.11                   |          |

E': Storage modulus | E: Elastic modulus |  $E_{pg}$ : Elastic modulus in pure glassy range |  $E_{gr}$ : Elastic modulus in glassy transition range |  $E_r$ : Elastic modulus of in rubbery zone.

of internal stresses and enthalpy relaxation around  $\theta_g$ . For the second heat, a CTE of 82 ppm/°C was noticed at around 16 °C and right after  $\theta_g$  a value of 298 ppm/°C was recorded. As stated before, the C-SMP is a semicrystalline type SMP whose crystallization effect started nearby 66 °C caused higher shrinkage and finished at 80 °C. The CTE seen after this crystallization range is 154 ppm/°C.

Similarly, Fig. 2b illustrates the first and second heat curves of A-SMP. In contrast to C-SMP, the A-SMP did not show any significant change in thermal expansion/shrinkage around  $\theta_g$  state. During the second heating cycle, a CTE of 73 ppm/°C and 233 ppm/°C were reported before and after glass transition zones. In addition, above  $\theta_g$  towards 81 °C a thermal expansion peak is noticed following a small shrinkage due to limited crystallinity in amorphous SMP. After molecules rearrangement around 110 °C, a CTE of 184 ppm/°C is noticed. Finally, both SMPs can lead to dimensional variations if kept heating

continuously at a higher temperature, i.e., a sudden drop near melting temperature of 156 °C is seen for A-SMP.

### 2.3. Physical analysis framework

A two-level design of experiment (DOE) approach was considered an appropriate tool to investigate the role of the same sets of printing variables on two distinct SMMs produced for 4D printing. In doing so, the Design-Expert software was used with the alike key objective to maximize the percentage shape recovery ratio as an output response (Table 5). This design approach can provide appropriate statistical and modeling techniques to evaluate the influencing factors, experimental results, and scrutiny of optimal parameters [10,16,29]. A total of sixteen experiments were appointed for optimizing the shape memory performance against printing variables (Table 3) namely, layer height,



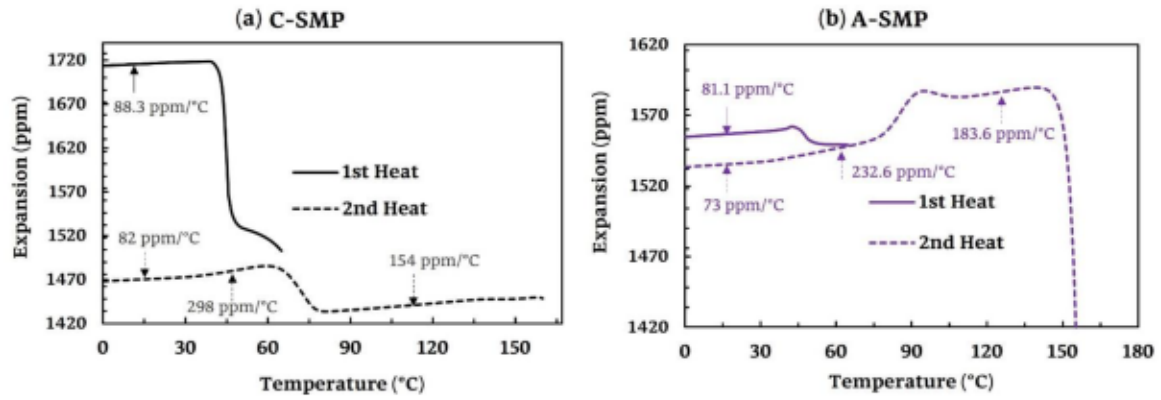


Fig. 2. Thermal expansion analyses on both SMPs by TMA (a) CTE curves of C-SMP (b) CTE curves of A-SMP.

Table 3

DOE factors and levels to study the shape memory effects.

| Factors            | Levels |      | Remarks  |
|--------------------|--------|------|----------|
|                    | Low    | High |          |
| Layer height       | 0.2    | 0.3  | mm (A)   |
| Nozzle temperature | 220    | 230  | °C (B)   |
| Printing speed     | 35     | 55   | mm/s (C) |

printing temperature, and speed as the major influencing parameters to regulate the 4D printed specimen's SMEs [10,18,30]. Similarly, these three parameters were the input factors of the DOE approach with 2-levels (low & high), and how they can affect the SMEs of the 4D printed intelligent device. In addition to a two-level design type, a three-factor interaction (3FI) design model was selected to study the inter-factorial interactions. Finally, knowing the lengthy thermo-mechanical SMEs, eight experiments and their predicted observation were planned for each material to estimate their SMEs under thermal stimuli as well as their corresponding interactions.

### 2.3.1. Design and printing of components

Geometric configuration is an important criterion to have the minimum failure of the structure and maximum energy absorption/dissipation capacity in terms of strain energy during the thermomechanical shape memory cycle (TSMC) [6,11,31]. Literature has demonstrated, increasing the thickness of the sample/cells improves the mechanical properties as well as the shape fixity ratio, however, the shape recovery ratio could reduce to a certain level due to high heterogeneous induced strain during the printing process, especially due to growth of stress-induced crystallization phases in the amorphous matrix [2,20]. In

this context, Sugiyama et al. [32] designed and fabricated four different lightweight core shapes, such as honeycomb, rectangle, circle, and rhombus while using a 3D printing technique. They reported the rhombus shape core had better mechanical properties, such as functional strength and stiffness than others. This indicates the rhombus design can store maximum strain energy in the hard segments which are responsible to perform shape recovery upon heating.

Therefore, out of different structures, a multicell rhombus-shape-structure (RSS) in the form of quadrilateral shapes with four equal side lengths and parallel opposite sides was selected and designed using Rhinoceros 3D to investigate the maximum shape programming and recovery ratios in this study (Fig. 3). Fig. 3a illustrate the unit cell rhombus structure whose  $3 \times 4$  multicell configuration (Fig. 3bc) can be served in multiple energy or shock-absorbing applications for 4D printing.

Overall, the RSS geometry is  $42 \times 33 \text{ mm} \times 9 \text{ mm}^3$  in size. A 9 mm thickness in the z-axis was assumed to have even layers during slicing (.stl format) and to be stable on the experimental platform for fixing during shape programming, either in compression or tensile tests. A closed chamber FFF based Volumic Stream 30-Ultra 3D printer with a standard 1.75 mm filament extruding facility was used to print the specimens of both SMPs. The unique set of printing parameters presented in Table 5 and estimated by a DOE approach for C and A SMPs were embedded to successfully print the testing specimens for maximum response factors. Rather than three variables discussed in this paper other constraints, such as typical printing parameters (infill type and percentage, raster angle, top/bottom solid layers, number of shells) and several other propositions discussed by Akbar et al. [10] were considered to fabricate such complicated structures even using smart and  $L\theta_g$  SMPs without posing additional challenges. Finally, Fig. 4 depicts the

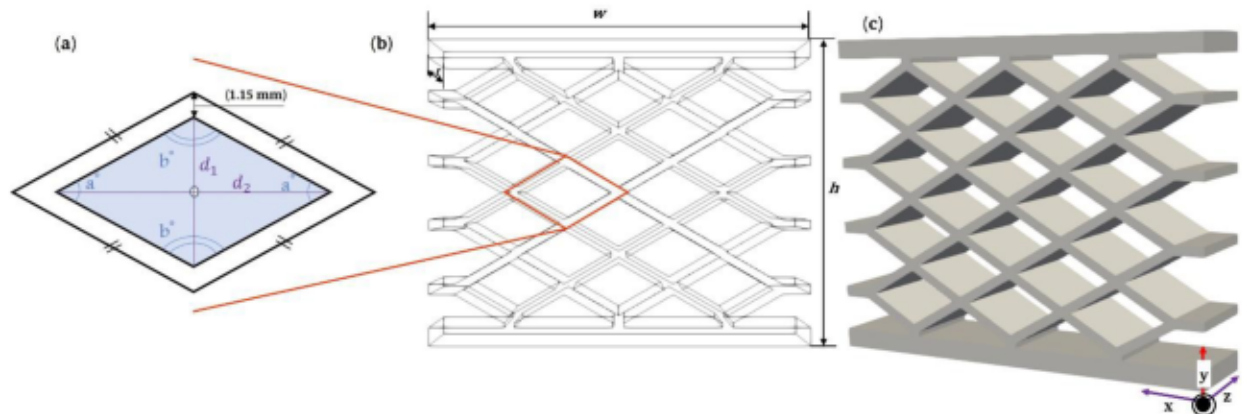
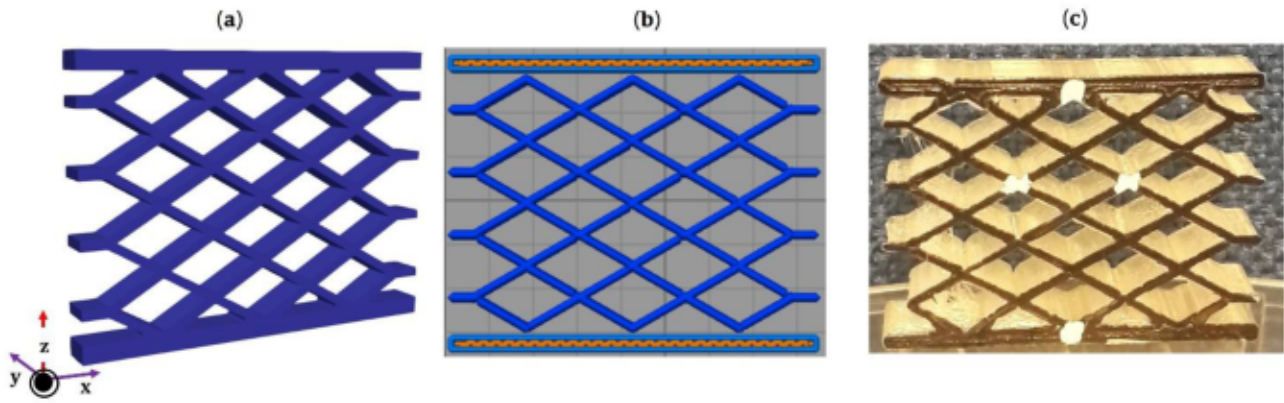


Fig. 3. Sample geometry for 4D printing (a) Single unit cell rhombus structure (b) Multiple unit cells schematic of RSS presenting 3D feature edges (c) 3D design of RSS exhibiting design axis.



**Fig. 4.** Sample schematics from design to 3D printing (a) 3D model of rhombus structure exhibiting compression testing axis (b) Sliced geometry for 3D printing (c) Physical printed SMP specimen.

design and 3D printing arenas of the RS structure.

### 2.3.2. Thermomechanical SME device

A second-generation non-contacting advanced video extensometer (AVE 2) by INSTRON® utilized to measure the precise strain contours under thermomechanical testing conditions. This advanced setup is equipped with an environmental chamber, and the complete setup is

mounted on a dual-column Universal Testing System acquired by INSTRON® (Fig. 5). Due to the complex nature of the specimen, a non-contacting AVE-2 instrument equipped with a highly precise environmental chamber was considered a suitable solution. The AVE-2 instrument works on the principle of digital image correlation (DIC) for strain measurements, where the reference configuration images are used to compare with the current configuration for post-analysis using DIC

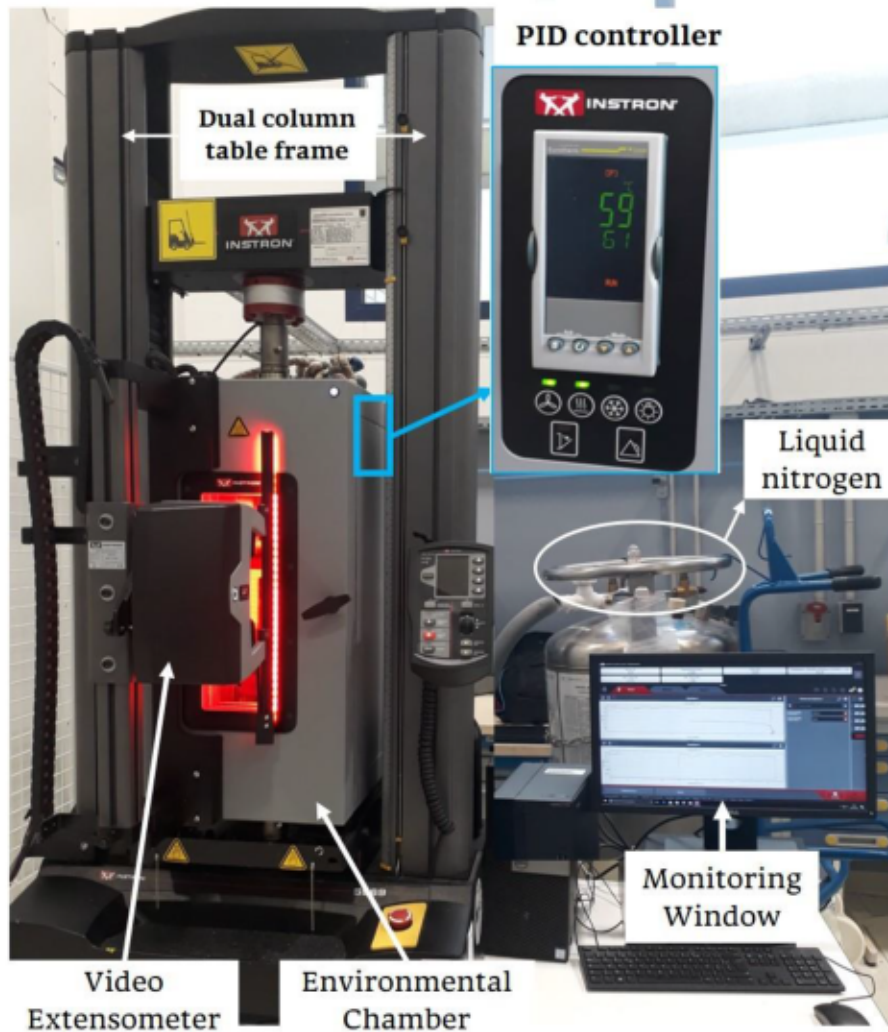


**Fig. 5.** Experimental setup to perform thermomechanical shape memory cycles.



replay software for full-field strain measurements.

In addition, the collective placement of an AVE-2 and controlled environmental chamber is a prime solution to account for any small change in strain storage or release in response to thermal stimuli [33]. AVE-2 can record every tiny recovery ratio that even started due to material or structural relaxation behavior before approaching to  $\theta_g$  of the polymers. This controlled environmental chamber presented in Fig. 5 has a forced convection heating system with a temperature homogenization fan and a liquid nitrogen system to cool the specimen from above  $\theta_g$  to near room temperature or even below  $-200^\circ\text{C}$  using a proportional integral derivative (PID) controller.

### 2.3.3. Thermomechanical SME cycle

The cycle of each design of the experiment run was performed for shape programming to 15% applied strain in the isothermal compression mode. Such deformations are helpful to account for multiple 4D printing functionalities but the amount of deformation should be controllable in the elastoplastic region for shape reversibility [16,26]. During the experimental preparation practice, every sample was placed on the fixed base plate of the INSTRON® testing machine according to the geometric testing axis shown in Fig. 4. In addition, the specimen was gripped firmly at room temperature with a 10 N initial fixation force. Finally, thermomechanical tests on 4D printed rhombus structures were performed while setting the output response factors from INSTRON® software, such as percentage longitudinal deformation, displacement in mm, time in seconds, force in N, % transverse deformation, and temperature in  $^\circ\text{C}$ . The complete thermomechanical cycle was done in a closed loop from the initial heating (step-1) to the final cooling (step-6) as illustrated in Fig. 6, and the related states of the experiments are simply described in Table 4.

The total induced strain accumulation is prone to heating/cooling instances developed during the printing process, during the thermomechanical SME cycle, and due to the structural design integrity of the specimen. Therefore, careful monitoring and controlling of the localized heating during shape programming and recovery is a key factor to trigger the best SMEs. To assume the temperature of the sample like the environmental chamber, a thermal equilibrium time of 2–3 min was maintained between each consecutive step (Table 4). This equilibrium time differentiates the thermomechanical cycle stages and provides enough relaxation time to stress/strain stability for 4D printed RSS during loading and unloading states. Table 4 and Fig. 6 present the overall thermomechanical conditions, equilibrium time, applied

stresses, corresponding SME behavior, heating, cooling, and loading rates of the SMC.

The polymer transition steps defined in Table 4 are the core of TMSMC under a controlled heating-cooling environment. All the SME cycles were programmed at a constant strain rate of  $2\text{ mm}\cdot\text{min}^{-1}$  to deform into a temporary form. An average heating/cooling rate of  $5^\circ\text{C}\cdot\text{min}^{-1}$  is recommended as an appropriate heating time factor for complete transitions of SMPs [1], hence it was considered in this research. The shape programming itself is influenced by the isothermal programming temperature, applied load, level of pre-stored strain, and cooling rate to fix the temporary shape. Although the shape recovery behavior is interconnected with temperature increase and recovered strain during a stress-free strain recovery process. Here between steps 4–5 of Fig. 6 as soon as the rising temperature increased linearly from  $\theta_g$  towards  $\theta_h$ , the recovery process was also begun linearly and speedily.

Therewith, Fig. 7 demonstrates the mechanical boundary conditions applied to deform the RSS for shape programming. For shape recovery, the removal of the upper gripper permits the unloading step, and the heating cycle enabled the release of the strain energy to successfully reconfigure the initial state of the specimen without external applied stress. Fig. 8 presents the physical illustration of the reversible reconfiguration of the RS structure under TMSMC following the similar six steps presented in Table 4. The green and red stages exhibit the sample at room temperature and above. It's possible to analyze from Fig. 8/stage-4 the qualitative structural configuration of RSS after shape programming, and Fig. 8/stage-6 the recovered reconfiguration of the structure. Notably, the recovered/regenerated shape of the RSS has shown that each cell was completely opened, which confirms the excellent shape memory and energy absorption capacity of the selected geometric structure and SMP materials. Overall, the working methodology to advance this study focuses on how the shape memory-affecting factors would perform within their thermomechanical extreme conditions concerning initial printed configurations.

## 3. Results and discussions

### 3.1. Shape memory effects (SMEs)

The rhombus-shape (RS) structures were fabricated according to a set of printing parameters discussed in Table 5, and their thermomechanical SMEs were investigated under the thermomechanical conditions prescribed in Table 4. A total of sixteen SMP samples were

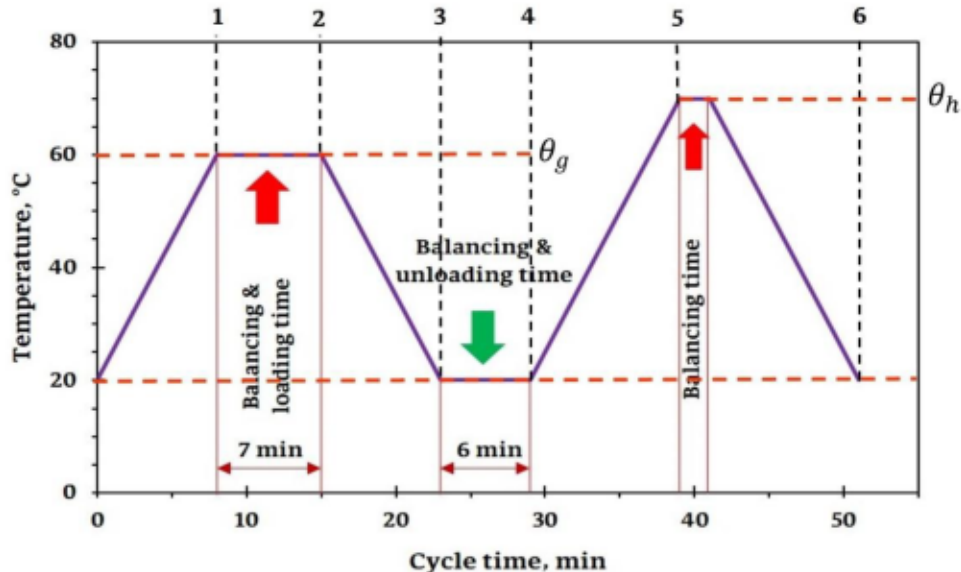


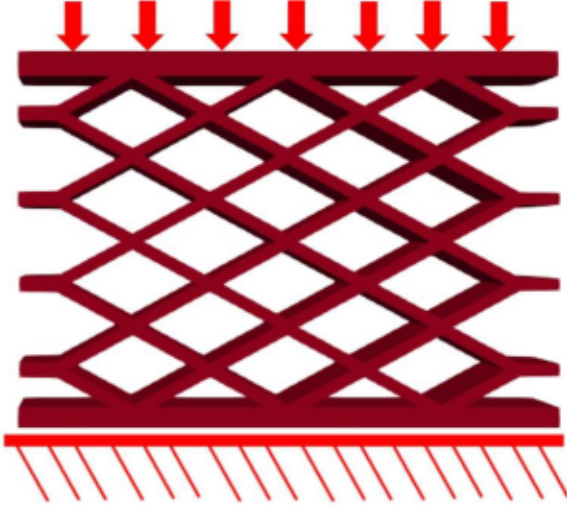
Fig. 6. Theoretical prediction of a thermomechanical cycle for SMP materials.



**Table 4**

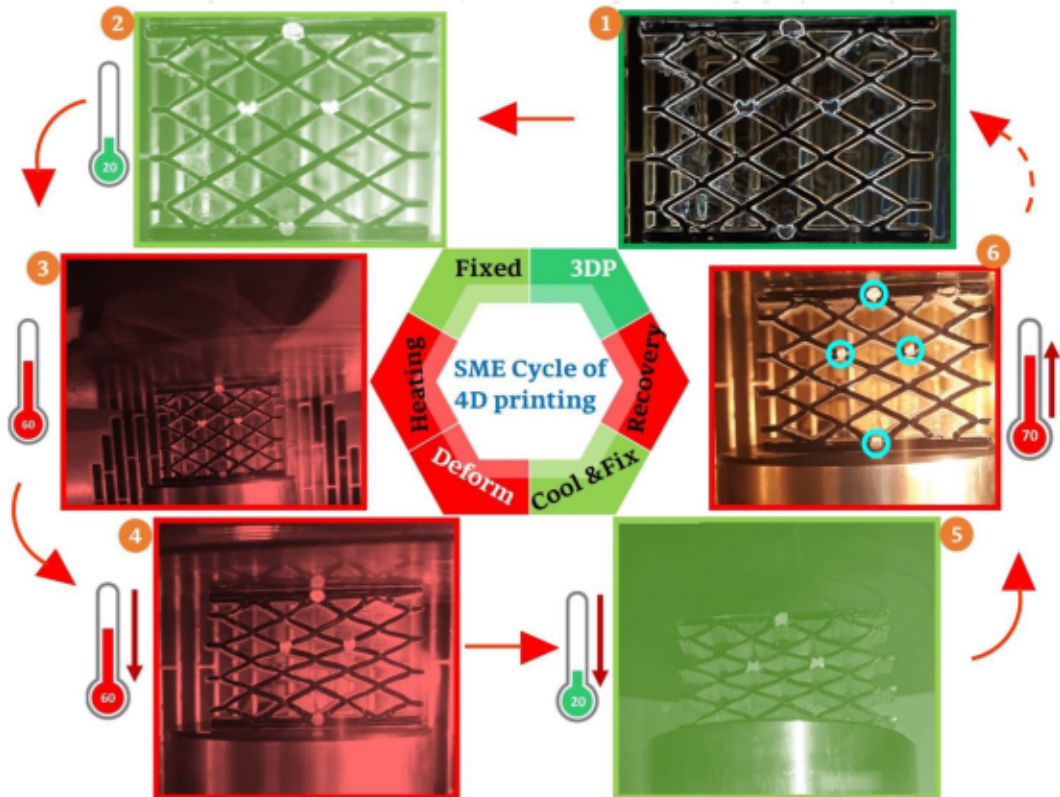
The quantitative trend of SME thermomechanical cycle performed in this study.

| No. | Step        | Temperature (°C) | Rate       | Equilibrium time (min) | Total step time (min) | Stress (MPa) | SME behavior                              |
|-----|-------------|------------------|------------|------------------------|-----------------------|--------------|---|
| 1   | Heating     | 20 → 60          | 5 °C/min   | 2–4                    | 10–12                 | 0.01         | Heating above $\theta_s$                  |
| 2   | Loading     | 60               | 2 mm/min   | 2–3                    | 6–7                   | 0.01–0.2     | Shape programming                         |
| 3   | 1st cooling | 60 → 20          | - 5 °C/min | 2–4                    | 10–12                 | 0.01         | Shape fixing                              |
| 4   | Unloading   | 20               | 2 mm/min   | 0–1                    | 2–3                   | 0.0          | Temporarily fixed shape for $R_f$ measure |
| 5   | Reheating   | 20 → 70          | 5 °C/min   | 2–4                    | 12–14                 | 0.0          | Shape recovery ratio                      |
| 6   | 2nd cooling | 70 → 20          | - 5 °C/min | 0                      | 10                    | 0.0          | Fixing of recovered shape                 |

**Fig. 7.** Mechanical boundary conditions to perform shape programming.

submitted to experimental cycles in the presence of the advanced setup presented in Fig. 5. This precisely controlled setup enabled maximum reversibility while releasing the stored strain homogeneously during the shape recovery phase of the thermomechanical cycle. The performance of the shape memory properties was measured while determining the strain release effects namely, shape recovery ratio ( $R_r$ )/Eq. 1 and strain locking effects shape fixity ratio ( $R_f$ )/Eq. 2 [30]. The  $R_r$  associated parameters are  $\epsilon_{int}$  and  $\epsilon_{rec}$ ; where  $\epsilon_{int}$  is the initial storage or programming strain which is represented in Fig. 9a phase-1 from start to 15% strain at 60 °C temperature. The  $\epsilon_{rec}$  is the recovered strain upon applied temperature stimuli as illustrated in Fig. 9a phase-3 from 15% → < 2% pointing < 100% of  $R_r$ . During the cooling phase after programming, the molecular chain mobility gets reduced to enable the storage of entropic energy in the system and perform the temporary shape fixity.  $R_f$  is the measure of material/structural rigidity to keep/fix the temporary form at room temperature after shape programming and unloading [2]. Where the  $\epsilon_{els}$  parameter of the  $R_f$  factor representing the elastic spring back recovered strain value just after unloading the specimen which can be noticed from Fig. 9a phase-2 at 20 °C temperature (mainly the  $R_f$  values of A-SMP are above 98% so the deviation in  $\epsilon_{els}$  is hard to predict visually).

$$R_r = 100\% - \frac{(\epsilon_{int} - \epsilon_{rec})}{\epsilon_{int}} \quad (1)$$

**Fig. 8.** The qualitative trend of experimental stages to perform thermomechanical shape memory cycles.

**Table 5**

SME results of C-SMP and A-SMP in reference to the printing parameters.

| DOE Run | A (mm) | B (°C) | C (mm/s) | Printing time (min) | Output response, $R_r$ (%) |              |
|---------|--------|--------|----------|---------------------|----------------------------|--------------|
|         |        |        |          |                     | C-SMP                      | A-SMP        |
| 1       | 0.3    | 220    | 55       | 25                  | 79.18 ± 0.95               | 85.18 ± 2.43 |
| 2       | 0.3    | 230    | 55       | 36                  | 75.77 ± 0.31               | 76.39 ± 1.30 |
| 3       | 0.2    | 230    | 35       | 37                  | 76.22 ± 0.31               | 74.76 ± 1.16 |
| 4       | 0.2    | 220    | 55       | 53                  | 77.72 ± 0.31               | 76.44 ± 1.56 |
| 5       | 0.2    | 230    | 55       | 53                  | 78.75 ± 0.30               | 71.49 ± 0.29 |
| 6       | 0.3    | 230    | 35       | 25                  | 82.40 ± 1.50               | 71.04 ± 0.30 |
| 7       | 0.3    | 220    | 35       | 36                  | 76.28 ± 0.23               | 81.82 ± 0.31 |
| 8       | 0.2    | 220    | 35       | 37                  | 79.96 ± 0.95               | 92.30 ± 0.32 |

 $R_r$  (%): Shape recovery ratio percentage.

$$R_f = \frac{\epsilon_{int}}{\epsilon_{els}} \times 100\% \quad (2)$$

During initial experimental efforts for shape programming on A-SMP material, a strain accumulation, and a time-dependent dimensional change/instability occurred at high temperatures even without applied loading, which was resolved with some mock trial-and-error tests to investigate the precise and formidable conditions for shape programming and recovery tests performed in this study. The C-SMP has shown better thermal stability at higher-end recovery temperatures even for longer resident/holding time than A-SMP. This is due to the ordered alignment of crystalline molecular chains (higher recrystallization above 70 °C) that withstand the loading direction over stretching or compressive modes. Any disordered and dimensional instability was not seen in all samples even having no additional curing, annealing, or physical aging treatments.

Table 5 enlists the experimental shape recovery results of C and A-SMPs for samples (1–8) fabricated under identical printing parameters and predicted by a high-order design model. The influence of irrecoverable strain in the initial cycle of both SMPs is higher (8–30 %), which is mainly due to heterogeneous strains induced from the printing process and difference in structural cells configuration for C and A SMPs, rather than the homogeneous pre-strain induced during shape programming. Therefore, the residual (irrecoverable) strain is responsible to stop the additional shape recovery due to the resistance of the hard distorted

segments in the polymer chains, which helps in the storage and release of strain energy during shape programming [2]. The optimal set of parameters in the case of C-SMP provided a maximum shape recovery ratio of 82–83% while around 92% in the case of A-SMP. The recovery percentages achieved and discussed in this study are comparable and some higher than recently reported data in the literature for nearly similar materials [14]. The average SME results of A-SMP are slightly higher (green highlights in Table 5) than C-SMP while printed and tested under identical settings. Notably, the C-SMP showed better results (red highlights in Table 5) when they were printed at a higher temperature (230 °C) than their manufacturer-recommended printing temperature range of 200–210 °C. In contrast, the A-SMP showed significantly higher results (up to 93%) whilst printed at a temperature (220 °C) than their manufacturer's given temperature of 195–210 °C, respectively. The other reasons for lower shape recovery ratios of C-SMP are due to the crystal destruction process during the higher pre-compressive strain of 15% on RSS which damages the existing physical crosslinking points responsible for shape memory effects. With the influence of printing parameters, the impact of recrystallization on C-SMP was higher than A-SMP which restricted the rearrangement of the deformed cells and limited the recovery ratio of C-SMP to a maximum of 82%.

Fig. 9 depicts the shape programming and recovery mechanism of both SMPs and the corresponding analyses are as followings;

- 1 Loading to perform shape programming at a constant 60 °C temperature for 4D printing in response to specific strain energy being stored in this stage. Fig. 9b1 presents the structural layout of physical deformation for shape programming.
- 2 Cooling to room temperature at  $-5\text{ }^{\circ}\text{C}\cdot\text{min}^{-1}$  while keeping the constant load. At this stage, stored pre-strain is locked to fix the programmed state of the object, and the initial shape fixity ratio is measured. At the end of this stage 2, it can be noticed (Fig. 9b2) the specimen is at room temperature withholding 15% of programmed pre-strain. The unloading step is also performed, and the final change in the value of the object due to elastic pushback (change in fixity ratio) is measured.
- Reheating above  $\theta_g$  until  $\theta_h$  (70 °C) enables the release of the stored pre-strain and recovery of the initial configuration as per the shape memory effects of the SMPs. During this phase, the elastoplastic residual strain should recover almost 100% [6]. At the end of this step, the difference in initial and final configuration enabled us to use the shape recovery formula ( $R_r$ ) and calculate the % recovery ratios.
- 3 Finally, to re-fix the recovered shape, the cooling back to room temperature (below  $\theta_g$ ) state has been performed to complete the polymer's thermomechanical SMC.

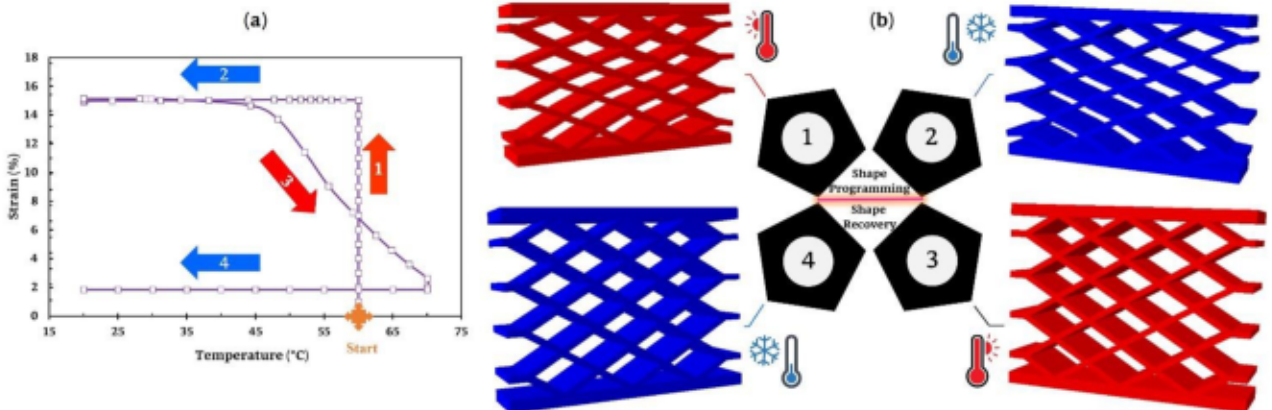


Fig. 9. Typical thermomechanical SMC (a) Strain versus temperature relationship recorded during experimental shape programming and recovery analyses (b) Physical behavior of RS structure during shape programming (1–2) and recovery stages (3–4).



### 3.2. 4D printing: experimental validation

To validate the experimental results the design-expert predictions were compared through analyses of variance. From the analysis of variance, the consequences of individual factors and their interaction on maximum shape recovery were examined. A three-factor interaction (3FI) design model was selected to interpret the impact of all factors. The ANOVA table (Table 6) is used to analyze the individual and collaborative influence of the three selected factors on the % shape recovery ratio as output, presented in Table 5. In Table 6, the F-value represents the influence level of individual and collective factors, and the *p*-value indicates whether the model is significant (*p*-value < 0.05) or not (*p*-value > 0.05). In the case of C-SMP, the parameter interactions such as ABC, AB, and BC ponders a greater impact on shape recovery percentage, while the individual contribution of parameters A and B was very low and therefore ignored in the ANOVA Table 6. In contrast, the A-SMP is highly affected by factor B and later by the interaction of AC and BC respectively. While the remaining parameters show limited influence on the shape recovery ratio. All ANOVA variables of C and A-SMP are significant, except the AB variable of the A-SMP factor which stayed non-significant. However, the higher degrees of AB in factor ABC maintained its significance.

In the meantime, the data correlation responses such as Predicted- $R^2$  and Adjusted- $R^2$  were obtained in the feasible range of having a difference of less than 0.2 which signifies that the model predicted and experimental results are very close to one another. In addition, the Adj- $R^2$  allowed us to check the data similarity while reducing the effect of non-significant terms and reported a very minor model error with 98.8% data similarity of C-SMP and more than 99% for A-SMP. The percentage contribution presented in Fig. 10 of the next section illustrates the parameter-wise and combine interactions to get optimal shape recovery values. The correlation of experimental and predicted data showed the results are very close to each other with  $R^2$  values above 99%. Finally, the data correlation and validation practices precisely measured any differences in the functional responses to analyze the influence of printing parameters and material variability. Reversibility check-ins of data collected through physical analytics and validated through a high-order design model predicted negligible errors.

### 3.3. Influence of printing parameters

The stress-free strain recovery properties of 4D-printed functional structures are highly dependent on printing parameters and the programming/recovery environment. The influence of printing parameters

directly controls the level of induced pre-strains, especially the heterogeneous induced strains on the deposition of every new layer. Usually, three types of residual strains are induced from the fabrication to the final 4D printing cycle; two are considered heterogeneous (the thermal-induced strains during deposition of layer-upon-layer in the printing process, and heat-induced strains during thermomechanical cycle steps; pre-heating and 1st cooling) and the third one is considered the homogeneous (compressive or tensile strains formed during shape programming phase). In this context, the design of experiments provided the relevant assessment of the optimum set of printing parameters influencing SMEs.

Fig. 10 presents the percentage contribution of individual and collective factors on relative shape recovery ratios. Fig. 10b reports the C-SMP is prone to maximum control over the  $R_r$  while combining the effects of all three printing parameters. Whereas factors AB (layer thickness, nozzle temperature) interaction on C-SMP has a 10% contribution as a second high interaction set, which enabled a maximum  $R_r$  of 82% of the first SME cycle in response to a layer thickness of 0.3 mm, nozzle temperature of 230 °C and minimum printing speed of 35 mm.s<sup>-1</sup> which is corresponding to DOE predicted run six. Factors BC (nozzle temperature, printing speed) interaction has shown an 8% contribution, the third highest interacting set out of all. Instead of factor AB influence, the interaction set BC reported 80%  $R_r$  while changing the nozzle temperature from 230 °C to 220 °C, layer height from 0.3 mm to 0.2 mm, and keeping the same printing speed (8th run).

Comparatively, Fig. 10c illustrates the major contributing factors and their percentage influence on A-SMP to regulate the shape recovery values. Surprisingly, factor B (nozzle temperature) had a significant effect on controlling the  $R_r$  percentage. This can be seen from its higher degree of interacting factors "F-value" namely AB, BC, and ABC. The A-SMP is an amorphous polymer and highly sensitive to temperature history and holding time at a high temperature which disturbs the arrangements of the molecular chain either during the printing process or SMC. Especially, for A-SMP the additional causes could be the viscoplastic effects. A higher nozzle temperature increase polymers melt flow, fusion bonding, and consequently the mechanical properties, however, due to increased fusion bonding the shape memory capacity of the molecular chains intends to reduce to a specific level, therefore, nozzle temperature has more severe effects on amorphous (A-SMP) than a crystalline (C-SMP). Furthermore, while keeping the factor AC (layer height, printing speed) interaction constant (a 26% contributor on A-SMP) and varying the nozzle temperature of DOE specimen A3 from 230 °C towards A8 of 220 °C has maximized the  $R_r$  to a 17% upwards (75% of A3 and 92% in event of A8 specimen).

**Table 6**  
Analysis of variance table of C-SMP and A-SMP to predict the individual effects.

| Material | Source   | Sum of squares | df | Mean square | F-value | p-value | Remarks     |
|----------|--|----------------|----|-------------|---------|---------|-------------|
| C-SMP    | Model  | 35.51          | 5  | 7.10        | 119.20  | 0.0083  | significant |
|          | C  | 1.48           | 1  | 1.48        | 24.88   | 0.0379  |             |
|          | AB   | 3.68           | 1  | 3.68        | 61.72   | 0.0158  |             |
|          | AC   | 2.02           | 1  | 2.02        | 33.85   | 0.0283  |             |
|          | BC   | 2.83           | 1  | 2.83        | 47.47   | 0.0204  |             |
|          | ABC  | 25.50          | 1  | 25.50       | 428.09  | 0.0023  |             |
|          | Residual   | 0.12           | 2  | 0.059       |         |         |             |
|          | Cor Total  | 35.63          | 7  |             |         |         |             |
|          | R <sup>2</sup> =0.9967 & Adj R <sup>2</sup> =0.9883; Predicted R <sup>2</sup> =0.94655 |                |    |             |         |         |             |
| A-SMP    | Model  | 373.12         | 6  | 62.19       | 1531.23 | 0.0196  | significant |
|          | B  | 221.03         | 1  | 221.03      | 5442.30 | 0.0086  |             |
|          | C  | 13.55          | 1  | 13.55       | 333.54  | 0.0348  |             |
|          | AB   | 1.06           | 1  | 1.06        | 26.06   | 0.1231  |             |
|          | AC   | 96.81          | 1  | 96.81       | 2383.84 | 0.0130  |             |
|          | BC   | 26.61          | 1  | 26.61       | 655.18  | 0.0249  |             |
|          | ABC  | 14.07          | 1  | 14.07       | 346.48  | 0.0342  |             |
|          | Residual   | 0.04           | 1  | 0.04        |         |         |             |
|          | Cor Total  | 373.16         | 7  |             |         |         |             |
|          | R <sup>2</sup> =0.9998; Adj R <sup>2</sup> =0.9992; Predicted R <sup>2</sup> =0.9930   |                |    |             |         |         |             |

A: layer height; B: Nozzle temperature; C: Printing speed.

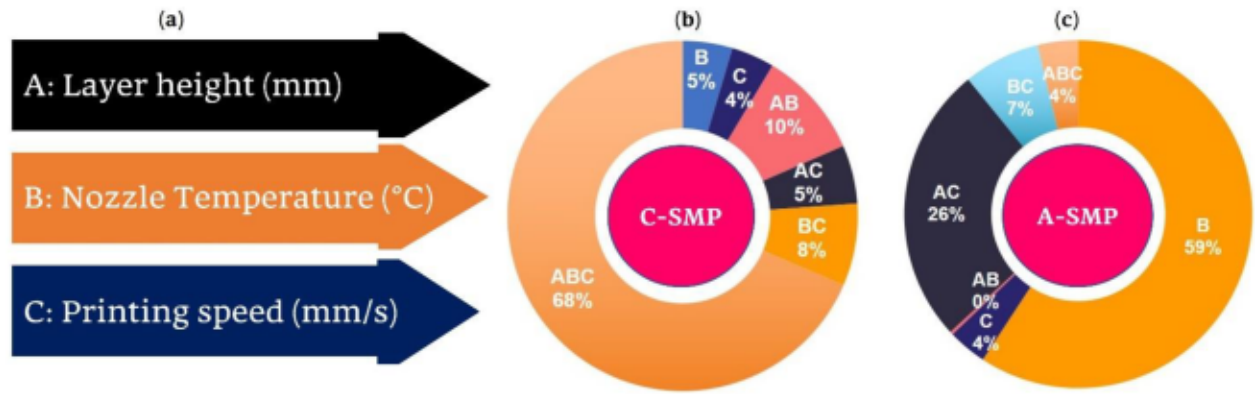


Fig. 10. Representation of printing parameters effects; individual and interactions (a) List of printing parameters used in this study (b) Interactions of C-SMP (c) Interactions of A-SMP.

The analysis of variance and percentage contribution charts indicates the output response ( $R_r$ ) sensitivity of C-SMP is belong to the relationship  $C > B > A$  where the factor C (printing speed) variation affected the recovery ratio more than other factors and the second leading factor is nozzle temperature. Literature reports, the effects of printing speed have a significant impact on altering the melt viscosity, object quality, and finally on shape memory response [16]. In contrast, the output response sensitivity of A-SMP is directed to relationship  $B > C > A$ , where factor B has the most significant role to increase or decrease the depending on the choice of the nozzle temperature range.

From the mentioned findings, the most effecting factor C on C-SMP and B on A-SMP and their low and high impacts are demonstrated in Fig. 11. Fig. 11a depicts the C-SMP response of  $R_r$  which is plotted

against factors A and B while considering the constant low ( $35 \text{ mm.s}^{-1}$ ) and high ( $55 \text{ mm.s}^{-1}$ ) values of factor C (printing speed). The 3D plot exhibits, the change in factor C from  $55$  to  $35 \text{ mm.s}^{-1}$  dramatically increased the output response to a high level. Fig. 11b outlines the A-SMP response of  $R_r$  plotted against factor A and C at constant values of factor B varying from  $220^\circ\text{C}$  to  $230^\circ\text{C}$ . A significant change in recovery ratio is seen i.e., maximum  $R_r$  at lower nozzle temperature ( $220^\circ\text{C}$ ) than at higher ( $230^\circ\text{C}$ ). Overall, the  $R_r$  is greatly influenced by the first SME cycle, which is prone to higher residual strains and an imperfect choice of printing parameters that generated further irrecoverable damage to the structure. Furthermore, the optimum  $R_r$  of C-SMP and A-SMPs can be computed and reassured with the perspective Eqs. (3 and 4) as given below. The equations in terms of coded factors are obtained from Design

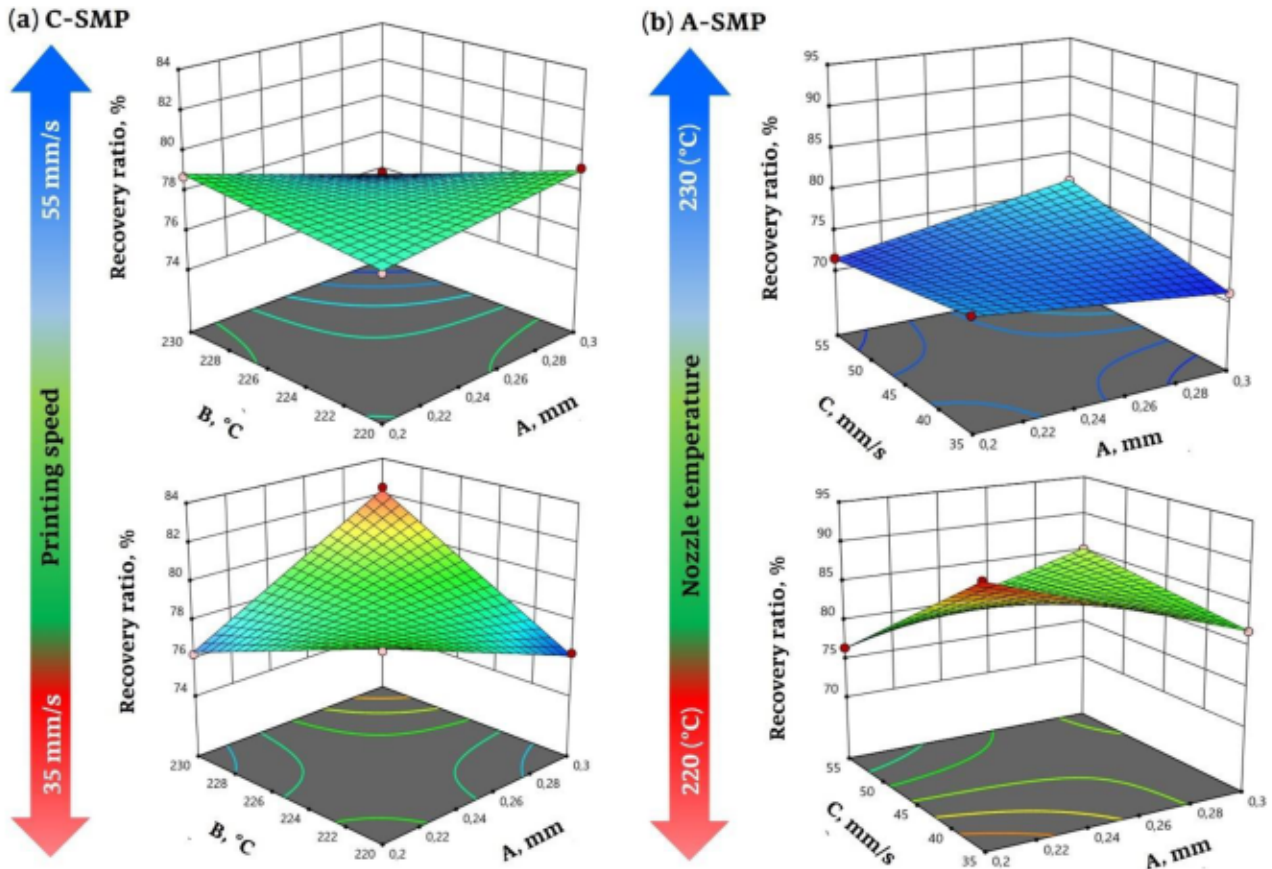


Fig. 11. The effects of maximum influencing parameters of both SMPs (a) Factor C effects at high and low printing speed (b) Factor B effects at high and low nozzle temperature.



Expert/ANOVA statistics to predict the response for given levels of each factor. These equations are useful to investigate statistically the process robustness and the relative impact of the factors (i.e., factors A, B, C) by comparing the factor coefficients. Where the high-level factors belong to positive coefficients (+1) and low-level to negative coefficient (−1) to present the increasing or decreasing trends of shape recovery ratios of the RSS.

$$C - SMP \rightarrow R_s = 78.29 - 0.4305C + 0.678AB - 0.502AC - 0.5945BC - 1.79ABC \quad (3)$$

$$A - SMP \rightarrow R_s = 78.68 - 5.26B - 1.3C + 0.3638AB + 3.48AC + 1.82BC - 1.33ABC \quad (4)$$

Moreover, Fig. 12 reports the results of individual factor interaction on percentage recovery ratio at 3-levels while varying the operating parameters given in Table 3 a to low, center point, and high level. As indicated above, the layer thickness has minimum effect on shape recovery response for C and A-SMP specimens, nevertheless, their least contribution is shown in petite plots where again the effects on C-SMPs are negligible and on A-SMP a bit evident. Overall in the case of the FFF printing process, a maximum layer thickness of 0.3 mm is completely safe in terms of surface finish, porosity, and mechanical properties as well. Secondly, a higher nozzle temperature increases the layers bonding, compactness, and homogeneity in the case of semi-crystalline

polymers (C-SMP), although a typical increase in  $R_s$  is also seen around 225 °C and then the decreasing trend. Similarly, the high nozzle temperature (230 °C) over-melted the A-SMP leading to thermal degradation and lower shape memory properties. While the maximum  $R_s$  of A-SMP at a nozzle temperature of 220 °C submitted to appropriate extrusion flow and melt pressure that enabled the smooth deposition and molecular chain alignments without distortions during the fabrication process.

Finally, the increase in printing speed has diminished the recovery ratio of C-SMP, although, this trend is the opposite in the case of A-SMP where the printing speed is the second high influencing factor with its high-order interacting factors AC, BC, and ABC. For A-SMP, an increase in printing speed with the combination of other factors (sample A1) increased the pre-strain in the deposited layers leading to better shape recovery%. Any difference in printing speed differs the stored pre-strain in the specimen, leading to a change in  $R_s$ . Overall, the results shown in Fig. 12 reported stronger interactions of A-SMP than C-SMP, especially, while varying the parameter nozzle temperature and printing speed. These consequences might be related to the level of induced strains that are interconnected to the  $R_s$  and are increasing simultaneously and linearly due to the thermo-elastic, viscoplastic, and viscoelastic behavior of A-SMP than its counterpart C-SMP. The induced programmed strains and their% recovery analyses by a single thermomechanical SMC showed higher shape memory properties of amorphous SMP than semi-crystalline in response to thermal stimuli.

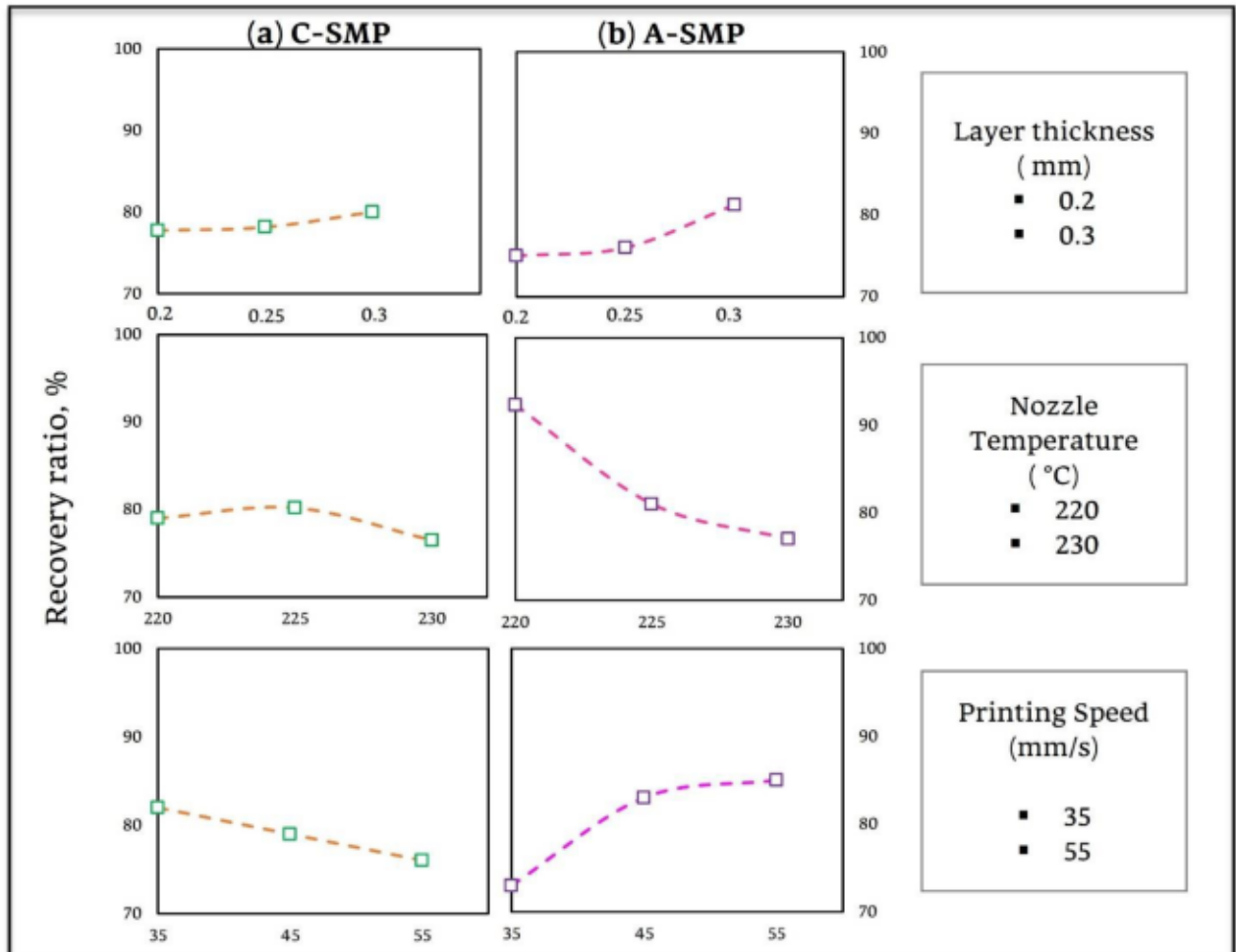


Fig. 12. Interaction curves of the recovery ratio percentage influenced by individual printing parameters.

### 3.4. Recovery ratio against time

Fig. 13 and Table 7 present the shape recovery ratio in response to instant and delayed recovery time (or structural relaxation time). Since strain transition in polymer arrangement is a time-temperature dependent process, mainly called volume relaxation, therefore, this phenomenon of holding time that can produce entirely different behavior due to stress relaxation is supported by the research community to acquire maximum  $R_r$  [15,25]. Here, instant recovery is when the gradually rising temperature (at  $5\text{ }^{\circ}\text{C}\cdot\text{min}^{-1}$ ) reached the defined end recovery temperature (i.e.,  $70\text{ }^{\circ}\text{C}$ ) and the delayed recovery means holding the end recovery temperature constant for 120 s after reaching this stage.

The graphical depiction of this extended recovery percentage after a delay of 120 s is shown in Fig. 9 (i.e., the vertical strain recovery line at  $70\text{ }^{\circ}\text{C}$ ) and the quantitative illustration (i.e., deviation) in  $R_r$  is shown in Fig. 13ab, and Table 7. The significantly higher extent of  $R_r$  percentage following a 2% higher recovery of C-SMP and about 5.88% higher  $R_r$  of A-SMP is computed while extending the heating delay for 120 s, shown in Table 7. The trend of getting a higher  $R_r$  on providing a heating delay of 120 s is positive regarding all C-SMP samples and six samples of A-SMP except A6 and A8, those have shown the least decrease. This might be due to the common lower printing speed of  $35\text{ mm}\cdot\text{s}^{-1}$  that increased the pronounced thermal effects during the printing process and lead to geometric instability in amorphous polymers against imbalance thermal interactions. The second reason could be the error in video extensometer tracking which might have lost the reference configuration points during experiments. The appropriate selection of holding time generates enough structural relaxation to experience maximum strain release and recovery ratios, respectively. Although, this is an experienced-based

knowledge that needs trials and tests to be identified properly, and some numerical computation may estimate the optimal cyclic timing framework.

In addition to the  $R_r$ , the percentage shape fixity ratio ( $R_f$ ) of all C and A SMPs is drawn in Fig. 13c. The shape fixity is measured after the release of programming stress and this shape fixation came because of viscous strains in nonequilibrium elements. Typically, the percentage  $R_f$  of both SMPs is well compliant with each other and higher than 94%. Furthermore, the A-SMP specimens showed a better  $R_f$ , i.e., the maximum deviation is seen in sample-7 where the A-SMP exhibited a 99.9%  $R_f$  in contrast to 95% of C-SMP. The lower  $R_f$  of C-SMP is linked to its semi-crystalline behavior that failed to provide enough resistance to the relaxation behavior of the compressed segments so their chains cannot slip back to a new length on the removal of programming load. The alternative reasons could be the higher pushback effects due to higher pre-strain induced during shape programming.

As discussed earlier (Fig. 10), the A-SMP is mainly affected by nozzle temperature therefore, in Fig. 14 we only reported the activation time and temperature influence on the  $R_r$  of A-SMP. It can be seen while heating the specimen from room temperature to above  $5\text{ }^{\circ}\text{C}\cdot\text{min}^{-1}$ , a slower activation has been started (at around  $40\text{ }^{\circ}\text{C}$ ) to perform the stress relaxation-based shape recovery even before reaching the actual computed  $\theta_g$  of  $55\text{--}60\text{ }^{\circ}\text{C}$ . All samples followed the linear recovery ratio relationship with their counter part-time and temperature scales, although, around the end recovery temperature of  $70\text{ }^{\circ}\text{C}$ , the vertical and horizontal increase shown in Fig. 14ab illustrate the rise in  $R_r$  that is belonged to a structural relaxation time of 120 s as indicated previously. Overall, the varying and longer recovery time of each A specimen has been subjected to a lower heating rate, higher-end recovery

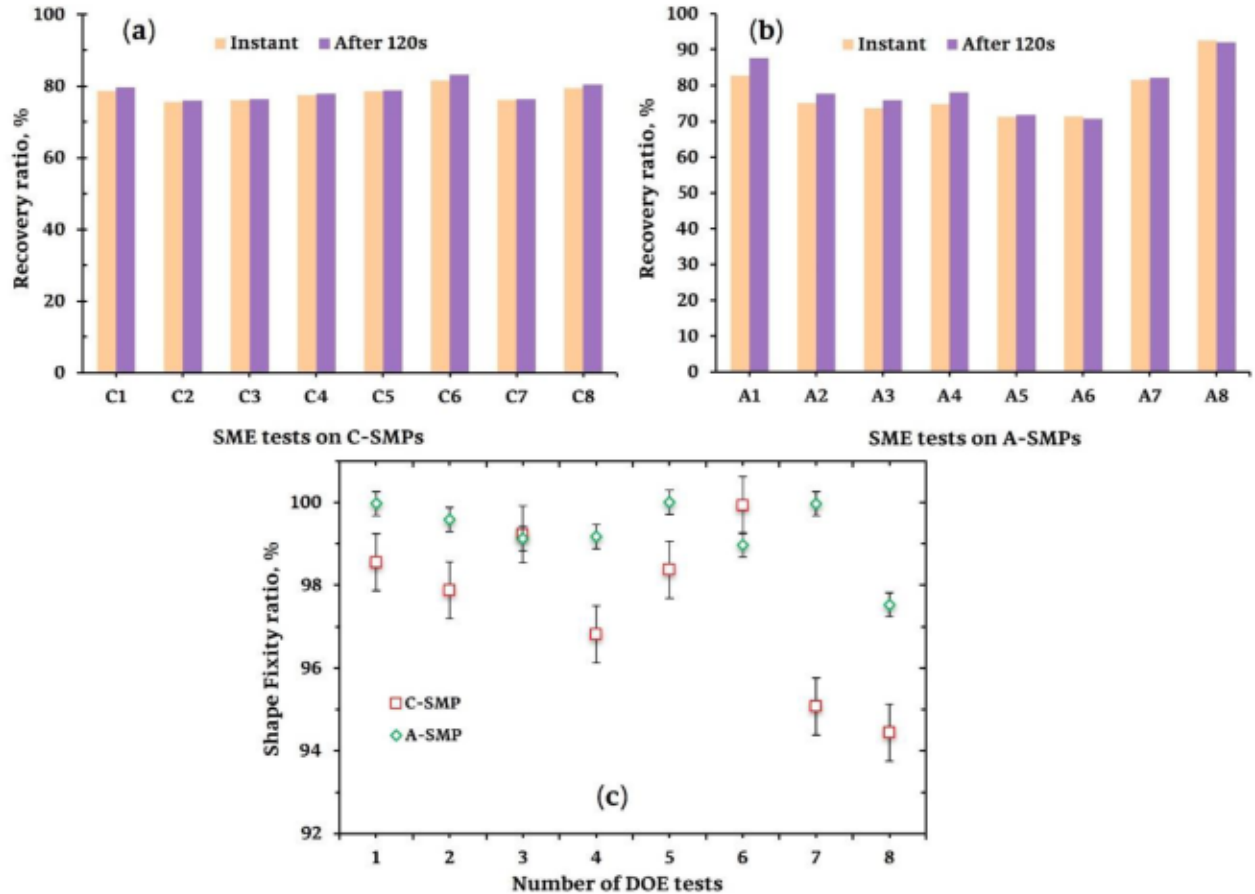


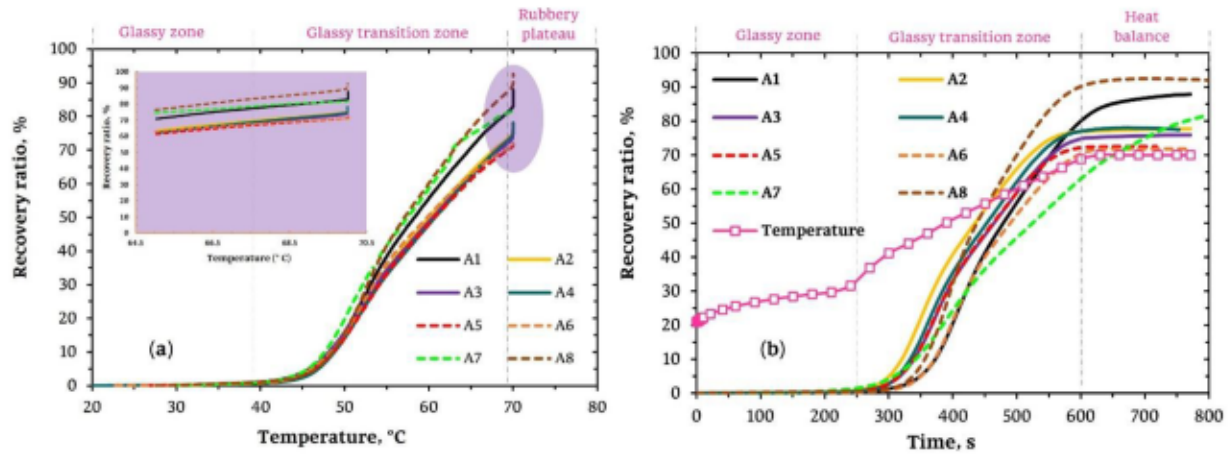
Fig. 13. Analysis of the% shape recovery and fixity ratios (a) Instant and delayed recovery of C-SMP (b) Instant and delayed recovery of A-SMP (c) Shape fixity ratios of C and A SMPs.



**Table 7**

Shape recovery analyses in reference to instant and delayed recovery times.

| Specimens | C-SMP             |                      |            | A-SMP             |                      |            |
|-----------|-------------------|----------------------|------------|-------------------|----------------------|------------|
|           | Instant recovery% | Recovery% after 120s | Deviation% | Instant recovery% | Recovery% after 120s | Deviation% |
| 1         | 78.71             | 79.66                | 1.20       | 82.75             | 87.62                | 5.88       |
| 2         | 75.62             | 75.93                | 0.41       | 75.09             | 77.70                | 3.47       |
| 3         | 76.07             | 76.38                | 0.40       | 73.59             | 75.93                | 3.17       |
| 4         | 77.57             | 77.88                | 0.40       | 74.87             | 78.01                | 4.19       |
| 5         | 78.60             | 78.90                | 0.39       | 71.20             | 71.78                | 0.81       |
| 6         | 81.66             | 83.14                | 1.81       | 71.35             | 70.73                | -0.87      |
| 7         | 76.17             | 76.40                | 0.30       | 81.51             | 82.14                | 0.77       |
| 8         | 79.49             | 80.43                | 1.18       | 92.62             | 91.97                | -0.70      |

**Fig. 14.** Time and temperature affect shape recovery behavior (a) Recovery ratio in function of temperature (b) Recovery ratio and time relationship of the thermo-responsive specimens.

temperature, and sets of printing parameters.

Fig. 15 presents the SMEs/recovery ratio vs. recovery time of A-SMP, it's noticeable the longer recovery time is not the only factor that affects maximum  $R_r$ %, but the influence of the variable printing parameters is also affecting considerably. Fig. 15a shows a higher recovery% with a few seconds of longer recovery time at a higher layer height of A1 than the counterpart A4 specimen. However, in Fig. 15b this trend was in contrast when computing the analyses with lower printing speed, in this setting, the sample printed with lower layer height and printing speed showed 8% better  $R_r$  and almost four minutes lower recovery time. In addition, the results presented in Fig. 15a and Fig. 15c were printed on exactly similar parameters except for the difference in printing temperature, here we can see the recovery time is almost in the similar range however, the  $R_r$  of A1 is 8% higher which was printed at 220 °C instead of A2 fabricated at 230 °C. A similar decline of a 4% lower recovery ratio is noticed for the A5 specimen printed at 230 °C rather than 220 °C in the case of A4.

Furthermore, an identical trend of printing at high temperatures with similar other parameters is drawn in Fig. 15d and the findings are interesting to compare with low-temperature printing drawn in Fig. 15b and other identical parameters. Meanwhile, it's interesting to see the samples fabricated at a higher printing speed of 55 mm.s<sup>-1</sup> (a & c) are corresponding to lower average recovery time and recovery ratio which is almost less than 400 s and 76.2%, whereas the fabrication of the samples at lower speed 35 mm.s<sup>-1</sup> (b & d) are submitted to a higher average recovery time and  $R_r$  that are 400 s and 79.6%, respectively. The recovery time trends of all A-SMP specimens are linear and increase with the increase in %  $R_r$ . These tendencies are a little flat with longer recovery times where the sets of parameters have lower printing speeds (i. e., A3 & A7). Since the A-SMP is highly sensitive to temperature change, therefore, the time, temperature history vs. recovery ratio curves of A-SMP are sketched, and C-SMP is ignored.

### 3.5. Shape programming strength

The shape programming of all RS structures was performed at an exceptionally slow constant strain rate (2 mm.min<sup>-1</sup>) inside a closed environmental chamber. The small strain rate and large peak strain of 15% were selected because the combination of both factors can enable maximum viscoelastic energy dissipation for better shape recovery of such intelligent structures for 4D printing. Fig. 16 illustrates the shape programming trends of the compression load vs. percentage deformation for the C and A-SMPs. Almost all compressive strength factors increase with the increase of peak strain towards 15% deformation. It's seen that the shape programming force around  $\theta_g$  (hot programming) is quite limited to a maximum of up to 30 N for the thermomechanical cycle of both SMPs. These findings are agreeable with the above  $\theta_g$  shape programming reported elsewhere. Whereas the cold programming (at ambient temperature) force on such a cellular structure was reported up to 600 N, which is evident from these SMPs temperature dependent properties discussed in the earlier sections of this paper. In Fig. 16a the increasing trend of the compressive strength is submitted to varying printing parameters where A1/A8 were fabricated at 0.3/0.2 mm layer height following the 55/35 mm.s<sup>-1</sup> printing speed. The blend of higher layer height and printing speed in the case of A1 increased the sample porosity/gap and consequently lowered the resulting compressive strength than A8. The rest of the specimens (A4/A7) presented identical findings; however, a slight difference was exhibited due to the sample fixing force at the beginning of the experiment. Fig. 16b shows the A specimens fabricated at a higher nozzle temperature (230 °C) with identical rest of the parameters as presented in Fig. 16a. The 50% lower compressive strength of A-SMPs shown in Fig. 16b has adhered to high-temperature printing that increased the printing and structural homogeneity; therefore, all specimens present the lowest differentiation in trends of compressive strength.

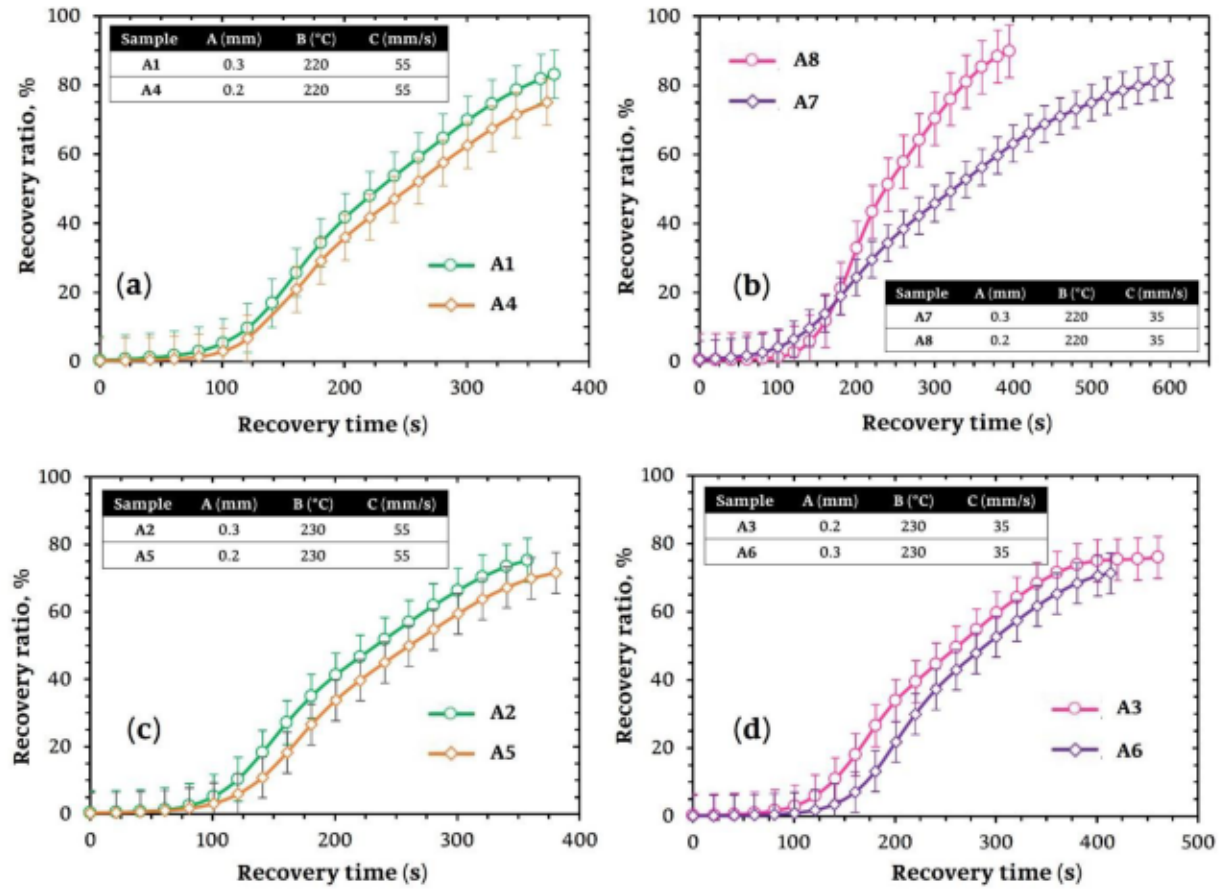


Fig. 15. Recovery ratio vs. recovery time graphs in the function of change in the single parameter (a & c) Printing with unique settings of higher printing speed except for nozzle temperature and layer height variation (b & d) Fabricated at lower printing speed and varying nozzle temperature (220 °C and 230 °C) and layer height.

Meanwhile, the compressive strength trend of C-SMP from Fig 16c illustrates a linear relationship except for C1, this linear behavior is a sign of the presence of crystallinity in this material as discussed earlier. A higher-degree crystalline material is prone to higher strengths, and better thermal stability than its counterpart A-SMP (amorphous polymer) which can be controlled by heat exposure, size of the crystal, and temperature rate. The other reasons for C-SMP to present higher compressive strength than A-SMP are due to significantly lower molecular mobility, and the addition of layer-by-layer gradual crystallinity in case of little heat imbalance. In addition, from Fig 16b, the difference in A3 and A6 compressive strength is linked with the increase of layer height from 0.2 to 0.3 mm, which is almost double and well correlated with the layer height effects on compressive strength reported by Barletta et al. [30]. Altogether, the average shape programming compressive strength of C-SMP is a bit larger than A-SMP which is due to the stronger intermolecular forces of this polymer as seen from the recrystallization effects by DMA. Finally, the proposed RS structure and their SMEs is interesting in a variety of energy-absorbing applications for 4D printing. Multiple energy-absorbing capabilities are possible while changing the cell size of this structure.

#### 4. Conclusion and perspectives

The shape memory-related features of two 4D-printed SMP materials were characterized and analyzed. Results indicated that C-SMP exhibits higher storage modulus (2.9 GPa) in the glassy range and lower  $\theta_g$  (52–57 °C) at 1 and 10 Hz in the glassy transition range. Although, A-SMP showed a lower storage modulus (1.9 GPa) in the glassy range and a higher  $\theta_g$  (57–61 °C). Secondly, a reconfigurable rhombus shape

structure was considered a potential shape for 4D printing applications in energy-absorbing robotics, aerospace, and biomedical devices. To master the shape memory effects of this structure, we identified the relevant printing and processing parameters namely, layer height, printing speed, and temperature. Methodologically, the data-driven shape programming of 4D printed objects was carried out in a compressive mode for 15% peak strain inside a precisely controlled environmental chamber. To drive the physical thermomechanical data for shape recovery behavior the printing speed affected most of the C-SMPs. In contrast, the nozzle temperature showed maximum impact on A-SMP, where a lower printing temperature introduced a higher shape recovery%, and a higher temperature diminished the% recovery up to 17%. Meanwhile, layer height reflects the least significant effects to control the shape recovery performance on both SMP materials. This study revealed the physics behind the processing parameters to understand what the most influencing parameter is to recover the initial configuration of the 4D-printed rhombus structure to build a structural part for dynamic energy-absorbing applications. Moreover, the shape recovery ratio at a holding time of 120 s was studied where the structural relaxation continues to grow the shape recovery percentage up to 6%. Such thermo-responsive SMPs need further attention to minimize the level of irrecoverable strains in the first cycle to strengthen the SMEs of amorphous and semicrystalline polymers. The data-driven multiple-SMCs are indispensable to knowing the strain accumulation, structural repetition, and fracture mechanism of such complex structures for 4D printing. Therefore, future research activities will include the investigation of SMEs under multiple thermomechanical SMCs on one or both SMPs.



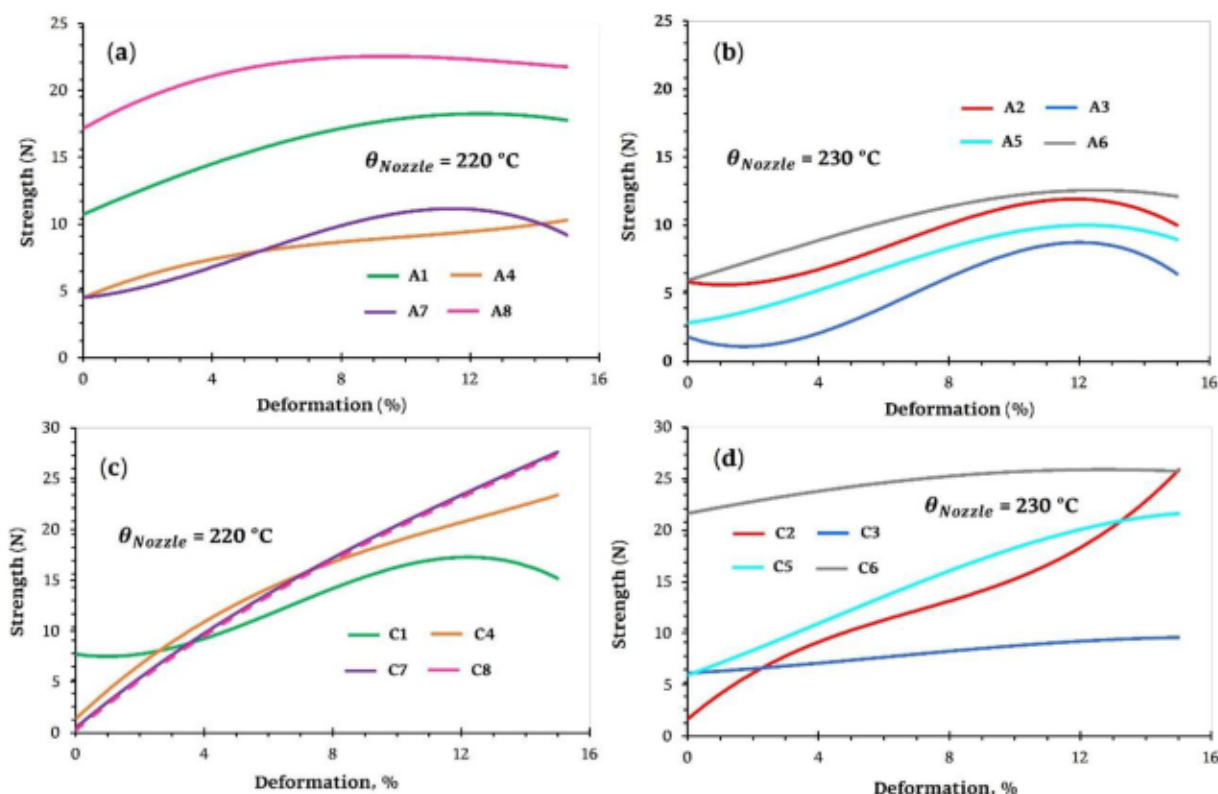


**Fig 16.** Shape programming compressive strength vs.% deformation tested at 60 °C (a) Compressive strength of four A-SMP samples printed at 220 °C (b) Compressive strength of four A-SMP samples printed at 230 °C (c) Compressive strength of four C-SMP samples printed at 220 °C (d) Compressive strength of four C-SMP samples printed at 230 °C.

#### CRedit authorship contribution statement

**Ijaz Akbar:** Conceptualization, Data curation, Investigation, Methodology, Software, Writing – original draft. **Mourad El Hadrouz:** Supervision, Formal analysis, Data curation, Writing – review & editing. **Mohamed El Mansori:** Supervision, Validation, Visualization, Project administration, Resources, Writing – review & editing. **Mostapha Tarfaoui:** Visualization, Resources, Formal analysis.

#### Declaration of Competing Interest

The authors declare that they have no known competing financial interests or personal relationships that could have appeared to influence the work reported in this paper.

#### Data availability

The data that has been used is confidential.

#### References

- [1] Q. Yang, G. Li, Temperature and rate dependent thermomechanical modeling of shape memory polymers with physics based phase evolution law, 2016. <https://doi.org/10.1016/j.ijplas.2015.09.005>.
- [2] A.J. Shahrol Azam Abdullaha, N.R. Abdullaha, L. Frommannb. Determination of Shape Fixity and Shape Recovery Rate of Carbon Nanotube-filled Shape Memory Polymer Nanocomposites, 2012, <https://doi.org/10.1016/j.proeng.2012.07.362>.
- [3] M. Mehrpouya, A. Gisario, A. Azizi, M. Barletta, Investigation on shape recovery of 3D printed honeycomb sandwich structure, *Polym. Adv. Technol.* 31 (2020) 3361–3365, <https://doi.org/10.1002/pat.5020>.
- [4] I. Akbar, M. El Hadrouz, M. El Mansori, D. Lagoudas, Toward enabling manufacturing paradigm of 4D printing of Shape Memory Materials: open literature review, *Eur. Polym. J.* 168 (2022), 111106, <https://doi.org/10.1016/j.eurpolymj.2022.111106>.
- [5] A.C. Pinho, C.S. Buga, A.P. Piedade, The chemistry behind 4D printing, *Appl. Mater. Today* 19 (2020), 100611, <https://doi.org/10.1016/j.apmt.2020.100611>.
- [6] M. Bodaghi, A. Serjouei, A. Zolfagharian, M. Fotouhi, H. Rahman, D. Durand, Reversible energy absorbing meta-sandwiches by FDM 4D printing, *Int. J. Mech. Sci.* 173 (2020), 105451, <https://doi.org/10.1016/j.ijmecsci.2020.105451>.
- [7] A. Kallel, M. Lamraoui, J. Fitoussi, A. Tcharkhtchi, The residual stress effect on the shape memory polymers, *Residual Stress 2* (2017) (2016) 151–156, <https://doi.org/10.21741/9781945291173-26>.
- [8] S. Djukic, A. Bocahut, J. Bikard, D.R. Long, Mechanical properties of amorphous and semi-crystalline semi-aromatic polyamides, *Heliyon* 6 (2020), <https://doi.org/10.1016/j.heliyon.2020.e03857>.
- [9] S.T. Ly, J.Y. Kim, 4D printing – fused deposition modeling printing with thermal-responsive shape memory polymers, *Int. J. Precis. Eng. Manuf.* 4 (2017) 267–272, <https://doi.org/10.1007/s40684-017-0032-z>.
- [10] I. Akbar, M. El Hadrouz, M. El Mansori, D. Lagoudas, Continuum and subcontinuum simulation of FDM process for 4D printed shape memory polymers, *J. Manuf. Process.* 76 (2022) 335–348, <https://doi.org/10.1016/j.jmapro.2022.02.028>.
- [11] C. Zeng, L. Liu, W. Bian, J. Leng, Y. Liu, Compression behavior and energy absorption of 3D printed continuous fiber reinforced composite honeycomb structures with shape memory effects, *Addit. Manuf.* 38 (2021), 101842, <https://doi.org/10.1016/j.addma.2021.101842>.
- [12] O. Testoni, T. Lumpe, J.L. Huang, M. Wagner, S. Bodkhe, Z. Zhakypov, R. Spolenak, J. Paik, P. Ermanni, L. Muñoz, K. Shea, A 4D printed active compliant hinge for potential space applications using shape memory alloys and polymers, *Smart Mater. Struct.* 30 (2021), <https://doi.org/10.1088/1361-665X/ac01fa>.
- [13] E. D'Elia, H.S. Ahmed, E. Feilden, E. Saiz, Electrically-responsive graphene-based shape-memory composites, *Appl. Mater. Today* 15 (2019) 185–191, <https://doi.org/10.1016/j.apmt.2018.12.018>.
- [14] F.V.-T. and M.B.N. Namvar, A Zolfagharian, elasto-plastic auxetic, hexagonal, and AuxHex structures fabricated by FDM 4D, (2022). <https://doi.org/https://doi.org/10.1088/1361-665X/ac6291> Reversible.
- [15] M. Aberoumand, K. Soltanmohammadi, E. Soleyman, D. Rahmatabadi, I. Ghasemi, M. Baniasadi, K. Abrinia, M. Baghani, A comprehensive experimental investigation on 4D printing of PET-G under bending, *J. Mater. Res. Technol.* 18 (2022) 2552–2569, <https://doi.org/10.1016/j.jmrt.2022.03.121>.
- [16] S. Mohammad, D. Tezerjani, M.S. Yazdi, M.H. Hosseinzadeh, The effect of 3D printing parameters on the shape memory properties of 4D printed polylactic acid circular disks : an experimental investigation and parameters optimization, *Mater. Today Commun.* 33 (2022), 104262, <https://doi.org/10.1016/j.mtcomm.2022.104262>.

- [17] J. Li, Z. Liang, X. Zhang, Q. Kan, Experimental investigation on the thermo-mechanical deformation of thermo-induced shape memory polyurethane, *Polymer* 237 (2021), 124337, <https://doi.org/10.1016/j.polymer.2021.124337>.
- [18] M. Mehrpouya, A. Azizi, S. Janbaz, A. Gisario, Investigation on the functionality of thermoresponsive origami structures, *Adv. Eng. Mater.* 22 (2020), <https://doi.org/10.1002/adem.202000296>.
- [19] C. Hao, K. Wang, Z. Wang, R. Duan, H. Liu, M. Huang, W. Liu, S. He, C. Zhu, Triple one-way and two-way shape memory poly(ethylene-co-vinyl acetate)/poly( $\epsilon$ -caprolactone) immiscible blends, *J. Appl. Polym. Sci.* 139 (2022) 1–10, <https://doi.org/10.1002/app.51426>.
- [20] Y. Wang, X. Li, An accurate finite element approach for programming 4D-printed self-morphing structures produced by fused deposition modeling, *Mech. Mater.* 151 (2020), 103628, <https://doi.org/10.1016/j.mechmat.2020.103628>.
- [21] Y. Zhang, L. Huang, H. Song, C. Ni, J. Wu, Q. Zhao, T. Xie, 4D Printing of a digital shape memory polymer with tunable high performance, *ACS Appl. Mater. Interfaces* 11 (2019) 32408–32413, <https://doi.org/10.1021/acsami.9b11062>.
- [22] T. Liu, L. Liu, C. Zeng, Y. Liu, J. Leng, 4D printed anisotropic structures with tailored mechanical behaviors and shape memory effects, *Compos. Sci. Technol.* 186 (2020), 107935, <https://doi.org/10.1016/j.compscitech.2019.107935>.
- [23] M. Han, Y. Yang, L. Li, Energy consumption modeling of 4D printing thermal-responsive polymers with integrated compositional design for material, *Addit. Manuf.* 34 (2020), 101223, <https://doi.org/10.1016/j.addma.2020.101223>.
- [24] Y. Huang, G. Dang, M. Zhu, L. Fan, M. Rong, M. Zhang, External stress-free reversible multiple shape memory polymer enabled by using broad melting range as equivalent multiple switching phases, *Appl. Mater. Today* 30 (2023), 101709, <https://doi.org/10.1016/j.apmt.2022.101709>.
- [25] M. Lei, K. Yu, H. Lu, H.J. Qi, Influence of structural relaxation on thermomechanical and shape memory performances of amorphous polymers, *Polymer (Guildf)* 109 (2017) 216–228, <https://doi.org/10.1016/j.polymer.2016.12.047>.
- [26] Y.Y.C. Choong, S. Maleksaeedi, H. Eng, S. Yu, J. Wei, P.C. Su, High speed 4D printing of shape memory polymers with nanosilica, *Appl. Mater. Today* 18 (2020), 100515, <https://doi.org/10.1016/j.apmt.2019.100515>.
- [27] ASTM, Standard Practice for Plastics: Dynamic Mechanical Properties: Determination and Report of Procedures, 2020. <https://www.astm.org/d4065-12.html> (Accessed 20 September 2022).
- [28] J.R.C. Dizon, A.H. Espera, Q. Chen, R.C. Advincula, Mechanical characterization of 3D-printed polymers, *Addit. Manuf.* 20 (2018) 44–67, <https://doi.org/10.1016/j.addma.2017.12.002>.
- [29] K. Wang, K. Engelbrecht, C.R.H. Bahl, Additive manufactured thermoplastic elastomers for low-stress driven elastocaloric cooling, *Appl. Mater. Today* 30 (2023), 101711, <https://doi.org/10.1016/j.apmt.2022.101711>.
- [30] M. Barletta, A. Gisario, M. Mehrpouya, 4D printing of shape memory polylactic acid (PLA) components: investigating the role of the operational parameters in fused deposition modelling (FDM), *J. Manuf. Process.* 61 (2021) 473–480, <https://doi.org/10.1016/j.jmapro.2020.11.036>.
- [31] H. Jiang, L. Le Barbenchon, B.A. Bednarczyk, F. Scarpa, Y. Chen, Bioinspired multilayered cellular composites with enhanced energy absorption and shape recovery, *Addit. Manuf.* 36 (2020), 101430, <https://doi.org/10.1016/j.addma.2020.101430>.
- [32] K. Sugiyama, R. Matsuzaki, M. Ueda, A. Todoroki, Y. Hirano, 3D printing of composite sandwich structures using continuous carbon fiber and fiber tension, *Compos. Part A Appl. Sci. Manuf.* 113 (2018) 114–121, <https://doi.org/10.1016/j.compositesa.2018.07.029>.
- [33] I. Akbar, M. El Hadrouz, M. El Mansori, M. Tarfaoui, Investigation of thermo-mechanical shape memory signatures of 3D printed and injection molded polymers, *CIRP J. Manuf. Sci. Technol.* 41 (2023) 277–291, <https://doi.org/10.1016/j.cirpj.2022.12.011>.